https://doi.org/10.5194/acp-2019-879
Preprint. Discussion started: 12 November 2019
© Author(s) 2019. CC BY 4.0 License.

Atmospheric Chemistry and Physics Discussions

Inverse modeling of SO_2 and NO_x emissions over China using multi-sensor satellite data: 1. formulation and sensitivity analysis

Yi Wang[1], Jun Wang[1,2], Xiaoguang Xu[2,3], Daven K. Henze[4], Zhen Qu[4]

[1]Interdisciplinary Graduate Program in Informatics, The University of Iowa, Iowa City, IA 52242, USA
[2]Department of Chemical and Biochemical Engineering, and Center for Global & Regional Environmental Research, The University of Iowa, Iowa City, IA 52242, USA
[3]Joint Center for Earth Systems Technology and Department of Physics, University of Maryland Baltimore County, Baltimore, Maryland, 21250, USA
[4]Department of Mechanical Engineering, University of Colorado Boulder, Boulder, CO 80309, USA

Correspondence to: Jun Wang (jun-wang-1@uiowa.edu) and Yi Wang (yi-wang-4@uiowa.edu)

Abstract. SO_2 and NO_2 observations from the Ozone Mapping and Profiler Suite (OMPS) sensor are used for the first time in conjunction with GEOS-Chem adjoint model to optimize both SO_2 and NO_x emission estimates over China for October 2013. OMPS SO_2 and NO_2 observations are first assimilated separately to optimize emissions of SO_2 and NO_x, respectively. Posterior emissions, compared to the prior, yield improvements in simulating columnar SO_2 and NO_2, in comparison to measurements from OMI and OMPS. The posterior SO_2 and NO_x emissions from separate inversions are 748 Gg S and 672 Gg N, which are 36% and 6% smaller than prior MIX emissions, respectively. In spite of the large reduction of SO_2 emissions over the North China Plain, the simulated sulfate-nitrate-ammonium Aerosol Optical Depth (AOD) only decrease slightly, which can be attributed to (a) nitrate rather than sulfate as the dominant contributor to AOD and (b) replacement of ammonium sulfate with ammonium nitrate as SO_2 emissions are reduced. Both data quality control and the weight given to SO_2 relative to NO_2 observations can affect the spatial distributions of the joint inversion results. When the latter is properly balanced, the posterior emissions from assimilating OMPS SO_2 and NO_2 jointly yield a difference of -3% to 15% with respect to the separate assimilations for total anthropogenic SO_2 emissions and ±2% for total anthropogenic NO_x emissions; but the differences can be up to 100% for SO_2 and 40% for NO_2 in some grid cells. Improvements on SO_2 and NO_2 simulations evaluated with OMPS and OMI measurements from the joint inversions are overall consistent with those from separate inversions. Moreover, the joint assimilations save ~50% of the computational time than assimilating SO_2 and NO_2 separately when computational resources are limited to run one inversion at a time sequentially. The sensitivity analysis shows that a perturbation of NH_3 to 50% (20%) of the prior emission inventory: (a) has negligible impact on the separate SO_2 inversion, but can lead to decrease of posterior SO_2 emissions over China by -2.4% (-7.0%) in total and up to -9.0% (-27.7%) in some grid cells in the joint inversion with NO_2; (b) yield posterior NO_x emissions over China decrease by -0.7% (-2.8%) for the separate NO_2 inversion and by -2.7% (-5.3%) in total and up to -15.2% (-29.4%) in some grid cells for the joint inversion. The large reduction of SO_2 between 2010 and 2013, however, only leads to ~10% decrease of aerosol optical depth regionally; reducing surface aerosol concentration requires the reduction of emissions of NH_3 as well.

1. Introduction

Both SO_2 and NO_2 in the atmosphere have adverse impacts on human health and can affect radiative forcing that leads to climate change. Not only do they cause inflammation and irritation of the respiratory system, but they also react with other species to form sulfate and nitrate aerosols (Seinfeld and Pandis, 2016), which subsequently can lead to or exacerbate respiratory and cardiovascular diseases (Lim et al., 2012). Sulfate and nitrate account for the largest mass of anthropogenic aerosols, which contributed to ~3 million premature deaths worldwide in 2010 (Lelieveld et al., 2015). In addition to health impacts, anthropogenic sulfate and nitrate are estimated to have caused -0.4 and -0.15 W m^{-2} radiative forcing, respectively, on a global scale between 1750 and 2011 through scattering solar radiation, and via modifying cloud microphysical properties (Myhre et al., 2013).

Satellite-derived global distributions of SO_2 and NO_2 Vertical Column Densities (VCDs) have been used to study the aforementioned impacts of SO_2 and NO_2 on atmospheric composition, climate change, and human health. In particular, since SO_2 and NO_2 VCDs are, to first order, linearly related to SO_2 and NO_x emissions (Calkins et al., 2016), they can be used to update bottom-up emission inventories that have large uncertainties and a temporal lag often of at least one year (Liu et al., 2018). Of particular interest for this study is China, which has large SO_2 and NO_x emissions from anthropogenic sources (coal-fired power plants, industry, transportation, and residential activity). Moreover, China has seen a 62% reduction in anthropogenic SO_2 emissions and a 17% reduction of anthropogenic NO_2 emissions on average from 2010 to 2017 (Zheng et al., 2018) due to the implementation of emission control policies, and these changes vary by regions, cities (Liu et al., 2016), and sectoral sources (Zheng et al., 2018). The reduction of SO_2 emissions mainly occurred in the coal-fired power plants and industry while it was largely ascribed to coal-fired power plants for NO_2 (Zheng et al., 2018). Noticeable uncertainties larger than 30% for both anthropogenic SO_2 and NO_x in 2010 over China were documented (Li et al., 2017b) and can be larger at the regional scale due to the uncertainty of activity rates, emission factors, and spatial proxies, which are

https://doi.org/10.5194/acp-2019-879
Preprint. Discussion started: 12 November 2019
© Author(s) 2019. CC BY 4.0 License.

used in the bottom-up approach (Janssens-Maenhout et al., 2015). Moreover, the large uncertainty is compounded by possible discrepancies caused by the temporal lag of bottom-up emission inventories and the rapid changes of emissions over time.

Several methods have been developed to update SO_2 and NO_x emissions using satellite VCD retrievals of SO_2 and NO_2, which have global coverage and near-real-time access. The mass balance method, which scales prior emissions by the ratios of observed VCDs to Chemistry Transport Model (CTM) counterparts, was applied to SO_2 retrievals from SCanning Imaging Absorption SpectroMeter for Atmospheric CHartographY (SCIAMACHY) and Ozone Monitoring Instrument (OMI) (Lee et al., 2011;Koukouli et al., 2018) and to NO_2 from Global Ozone Monitoring Experiment (GOME) and OMI (Martin et al., 2003;Lamsal et al., 2010) to estimate SO_2 and NO_x emissions, respectively. Lamsal et al. (2011) simulated the sensitivity of VCDs to emissions (the finite difference mass balance approach) using a CTM, which was applied to OMI NO_2 retrievals to estimate NO_x emissions. SO_2 VCD retrievals from GOME, GOME-2, SCIAMCHY, and Ozone Mapping and Profiler Suite (OMPS) were used to estimate point sources through linear regression between VCDs and emissions or function fitting, although the method can only detect about half of the total anthropogenic SO_2 emissions (Li et al., 2017a;Zhang et al., 2017;Fioletov et al., 2013;Fioletov et al., 2016). With explicit considerations of chemistry, transport, and deposition, the four-dimension variational data assimilation (4D-Var) approach was applied to estimate emissions using SO_2 data from OMI (Wang et al., 2016;Qu et al., 2019a), and NO_2 data from SCIAMCHY, GOME-2, and OMI (Kurokawa et al., 2009;Qu et al., 2017;Kong et al., 2019). The 4D-Var posterior has a smaller root mean square error than the mass balance posterior, especially in the conditions when the initial guess and true emissions have different spatial patterns (Qu et al., 2017); this is because the spatial extent of source influences on modelled column concentrations (Turner et al., 2012) are only indirectly accounted for in the mass balance approach. Cooper et. al (2017), however, showed that the iterative finite difference mass balance approach has similar accuracy as the 4D-Var approach for global-scale models with coarse resolution. To combine the strengths of the 4D-Var and mass balance approaches, Qu et al. (2017) further introduced a hybrid 4D-Var-mass-balance approach, which can better capture trends and spatial variability of NO_x emissions than the mass balance approach and save significant computational resources when applied to constrain monthly NO_x emissions for multiple years. Other data assimilation approaches including the ensemble Kalman filter method (Miyazaki et al., 2012;Miyazaki et al., 2017) and the Daily Emission estimates Constrained by Satellite Observation (DECSO) algorithm (Mijling and van der A, 2012;Ding et al., 2015) have also been used to constrain NO_x emissions.

https://doi.org/10.5194/acp-2019-879
Preprint. Discussion started: 12 November 2019
© Author(s) 2019. CC BY 4.0 License.

Here, we focus on the development and feasibility for joint 4D-var assimilation of satellite-based SO_2 and NO_2 data to optimize SO_2 and NO_x emission strengths simultaneously. Specifically, this study aims to conduct 4D-Var assimilation of VCDs of SO_2 and NO_2 from OMPS to constrain SO_2 and NO_x emissions over China using the GEOS-Chem 4D-Var inverse modeling framework. In our companion study (Wang et al., 2019), we develop approaches to downscaling the optimized emission inventories for improving air quality predictions. Despite their numerous applications for top-down estimate of SO_2 and NO_x emissions in the past two decades, GOME and SCIAMCHY stopped providing data in 2004 and 2012, respectively, while OMI has been suffering from a row anomaly that leads to much less spatial coverage and larger data uncertainty (Schenkeveld et al., 2017). Hence, it is important to study the potential of next-generation sensors such as OMPS toward continuously monitoring the change of SO_2 and NO_x emissions and their atmospheric loadings. Two OMPS sensors onboard Suomi NPP and NOAA-20 have been launched in 2011 and 2018, respectively, and the third one is expected to be launched in 2020. As OMPS will continue to provide SO_2 and NO_2 retrievals in the next two decades, this study seeks to provide a critical assessment of the extent to which the OMPS observations improve emissions estimates and air quality forecast at the regional scale for the first time.

The novelty of this study lies not only in the first application of OMPS SO_2 and NO_2 retrievals to constrain emissions using the 4D-Var technique but also in the deployment of OMI data to assess the GEOS-Chem simulation with posterior emissions, thereby studying the degree to which OMPS and OMI retrievals, despite their difference in sensor characteristics and inversion techniques, can provide consistent constraints for the model improvement. Qu et al. (2019a) showed that posterior SO_2 emissions from different OMI SO_2 products vary in strength and have consistent trend signs. Our study here using OMPS thus touches an important issue, which is whether or not there would be any artificial trends in our climate data record of atmospheric SO_2 and NO_2 due to the transition of satellite sensors. Our study is also different from past studies (Wang et al., 2016;Qu et al., 2017;Qu et al., 2019a;Qu et al., 2019b) that have applied the 4D-Var technique to OMI data with the GEOS-Chem adjoint model, but did not include evaluation with independent satellite data. Qu et al. (2019b) showed joint inversion using OMI SO_2 and NO_2 benefits from simultaneous adjustment of OH and O_3 concentrations, which supports assimilating OMPS SO_2 and NO_2 observations simultaneously in this study. Additionally, considering that the uncertainty of NH_3 emission inventories is up to 153% over China (Kurokawa et al., 2013) and NH_3 emissions are not constrained in our inversions, we also explore issues related to the co-variation among species that appear

https://doi.org/10.5194/acp-2019-879
Preprint. Discussion started: 12 November 2019
© Author(s) 2019. CC BY 4.0 License.

to be independent but indeed are connected through chemical processes and analyze the differences in responses of emissions and aerosols to NH_3 emissions uncertainty between joint and single-species assimilations.

We describe OMPS and OMI data in Sect. 2. The GEOS-Chem model and its adjoint as well as the design of numerical experiments are presented in Sect. 3. Results of case studies for October 2013 are provided in Sect. 4. Sect. 5 consists of discussion and conclusions.

2. Data

2.1 OMPS data as constraints

We use OMPS Level-2 SO_2 and NO_2 tropospheric VCDs in October 2013 as constraints to optimize SO_2 and NO_x emissions over China. The OMPS nadir mapper on board the Suomi-NPP satellite, launched in November 2011, observes hyperspectral solar radiance and earthshine radiance at 300-380 nm (Flynn et al., 2014). With 35 detectors of 50x50 km nominal pixel size in cross-track direction, OMPS has a swath of 2800 km flying across the equator at 1:30 PM local time ascendingly at the sunlit side of the Earth surface and providing global coverage daily. Both SO_2 and NO_2 are retrieved through the Direct Vertical Column Fitting (DVCF) algorithm with SO_2 and NO_2 atmospheric profile information from GEOS-Chem simulations and have a retrieval precision of 0.2 DU and 0.011 DU, respectively (Yang et al., 2013;Yang et al., 2014).

Only pixels with both Solar Zenith Angle (SZA) and View Zenith Angle (VZA) less than 75° are used, as larger SZA or VZA result in longer light path length, and consequently less information content and lower data quality for retrieving the change of SO_2 or NO_2 loadings in the Plane Boundary Layer (PBL) where the two trace gases from anthropogenic sources mainly concentrate. We also remove the pixels with Radiative Cloud Fraction (RCF) larger than 0.2 for SO_2 and 0.3 for NO_2 as a trade-off between the data amount and cloud impacts. Considering their large uncertainty, OMPS SO_2 retrievals in the grid cell where the prior simulation is less than 0.1 DU will not be used, except in Quality Control (QC) sensitivity analysis experiments.

2.2 OMI data for assessment

OMI Level-3 SO_2 and NO_2 tropospheric VCDs at a spatial resolution of 0.25°x0.25° from NASA are used for evaluating the model results. OMI is a UV-vis hyperspectral sensor that observes solar irradiance and earthshine radiance at 300-500 nm. The swath of OMI is 2600 km, consisting of 60 detectors with the nominal pixel size of

https://doi.org/10.5194/acp-2019-879
Preprint. Discussion started: 12 November 2019
© Author(s) 2019. CC BY 4.0 License.
Atmospheric Chemistry and Physics Discussions

13x24 km^2 at nadir. OMI flies across the equator in the ascending node at 1:45 PM local time, which is very close to the 1:30 PM local time for OMPS. Due to row anomaly (Schenkeveld et al., 2017), OMI takes more than one day to provide global coverage. The Level-3 product is derived from the Level-2 product; the latter is retrieved through the Principal Component Analysis (PCA) algorithm with a fixed Air Mass Factor (AMF) assumption for SO_2 (Li et al., 2013) and variation of the Differential Optical Absorption Spectroscopy (DOAS) algorithm for NO_2 (Krotkov et al., 2017;Marchenko et al., 2015), with a precision of 0.5 DU (Li et al., 2013) and 0.017 DU (Krotkov et al., 2017), respectively. In the Level-3 product, pixels affected by row anomaly are removed. For SO_2, only the pixel with the shortest light path, SZA less than 70°, RCF less than 0.2, and detector number in the range of 2 to 59 (1-based) is retained in a 0.25°x0.25° grid cell and then corrected with a new AMF based on GEOS-Chem SO_2 profile simulation (Leonard, 2017). For the OMI Level-2 NO_2 product, the AMF calculation is based on Global Modeling Initiative NO_2 profile simulation (Krotkov et al., 2017), and all pixels with SZA less than 85°, terrain reflectivity less than 30°, RCF less than 0.3 are averaged in a 0.25°x0.25° grid cell weighted by the overlapping area of grid cell and pixel to form Level-3 product (Bucsela et al., 2016). In the assessments, OMI observations are averaged at 2°x2.5° model grid cell, and model simulations are sampled by OMI observational time.

3. Method

3.1 GEOS-Chem and its adjoint

GEOS-Chem is a 3-D chemistry transport model driven by emissions and GEOS-FP meteorological fields. The secondary sulfate-nitrate-ammonium aerosol formation in the model is introduced by Park et al. (2004). Both aerosols and gases are removed by wet deposition, including washout and rainout from large-scale or convective precipitation (Liu et al., 2001) and the dry deposition following a resistance-in-series scheme with aerodynamic resistance and boundary resistance calculated from GOES-FP meteorological field and surface resistances based largely on a canopy model (Wang et al., 1998;Wesely, 1989). Anthropogenic SO_2, NO_x, and NH_3 emissions used over East Asia are the mosaic emission inventory (MIX) (Li et al., 2017b) for year 2010. SO_2 and NO_2 VCDs are simulated at 2°x2.5° resolution with 47 vertical layers using both the prior and posterior emission inventories to compare with OMI retrievals.

https://doi.org/10.5194/acp-2019-879
Preprint. Discussion started: 12 November 2019
© Author(s) 2019. CC BY 4.0 License.

The GEOS-Chem adjoint model is a tool for efficiently calculating the sensitivity of a scalar cost function with respective to large numbers of model parameters simultaneously such as emissions (Henze et al., 2007). In this study, the cost function is defined as Eq. (1).

$$J(\boldsymbol{\sigma}) = \gamma\frac{1}{2}\left[H_{SO2}\left(M(\boldsymbol{\sigma})\right) - \mathbf{c}_{SO2}\right]^{T}\mathbf{S}_{SO2}^{-1}\left[H_{SO2}\left(M(\boldsymbol{\sigma})\right) - \mathbf{c}_{SO2}\right] + \frac{1}{2}\left[H_{NO2}\left(M(\boldsymbol{\sigma})\right) - \mathbf{c}_{NO2}\right]^{T}\mathbf{S}_{NO2}^{-1}\left[H_{NO2}\left(M(\boldsymbol{\sigma})\right) - \mathbf{c}_{NO2}\right] + \frac{1}{2}[\boldsymbol{\sigma} - \boldsymbol{\sigma}_a]^{T}\mathbf{S}_a^{-1}[\boldsymbol{\sigma} - \boldsymbol{\sigma}_a] \quad (1)$$

E is a vector in which SO_2 and NO_x emissions are ordered by GEOS-Chem model grid cell and by species. $\mathbf{E}_a$ is a prior estimate, and $\boldsymbol{\sigma}$ is a state vector, consisting of $\ln(E_i/E_{a,i})$, where E_i and $E_{a,i}$ are the i^{th} element in **E** and $\mathbf{E}_a$, respectively. $\mathbf{c}_{SO2}$ and $\mathbf{c}_{NO2}$ are vectors of OMPS SO_2 and NO_2 tropospheric VCDs, respectively. $\mathbf{S}_{SO2}$ and $\mathbf{S}_{NO2}$ are observation error covariance matrixes for SO_2 and NO_2 and are assumed to be diagonal, which means observational errors are uncorrelated. M is the GEOS-Chem model that simulates the relationship between SO_2 and NO_2 concentrations in the atmosphere and the emissions factors. H_{SO2} and H_{NO2} are observation operators which map GEOS-Chem simulations of SO_2 and NO_2 to the observational space, respectively. $\boldsymbol{\sigma}_a$ is the prior estimate of $\boldsymbol{\sigma}$, and $\mathbf{S}_a$ is the error covariance matrix for $\boldsymbol{\sigma}_a$. $\mathbf{S}_a$ is assumed to be diagonal with a relative error of 50% for SO_2 and 100% for NO_x as used in Xu et al. (2013). γ is a parameter we introduce to balance the importance of the SO_2 observation term (first term on the right side of Eq. (1)) and NO_2 observational term (second term on the right side of Eq. (1)), given both the different sizes and observation errors of these two observation datasets.

OMPS SO_2 and NO_2 tropospheric VCDs can be directly compared to GEOS-Chem tropospheric VCDs of SO_2 ($H_{SO2}\left(M(\boldsymbol{\sigma})\right)$ in Eq. (1)) and NO_2 ($H_{NO2}\left(M(\boldsymbol{\sigma})\right)$ in Eq. (1)). Retrieving satellite SO_2 and NO_2 tropospheric VCDs requires assumptions regareding SO_2 and NO_2 vertical profiles, as the sensitivity of the radiance observed by satellite sensors to the changes of SO_2 or NO_2 loadings is a function of plume height. If the vertical profile assumptions in the retrieval process are inconsistent with the GEOS-Chem simulations, the inconsistency partly contributes to the difference between the GEOS-Chem simulations and the OMPS retrievals ($H_{SO2}\left(M(\boldsymbol{\sigma})\right) - \mathbf{c}_{SO2}$ or $H_{NO2}\left(M(\boldsymbol{\sigma})\right) - \mathbf{c}_{NO2}$). In this study, OMPS SO_2 and NO_2 tropospheric VCDs are retrieved using the shape of vertical profiles from GEOS-Chem simulations (Yang et al., 2013;Yang et al., 2014), although differences of model version, simulation year, and emission inventory still exist. Hence, the difference between the GEOS-Chem simulations and the OMPS retrievals is mostly ascribed to the uncertainty of the emissions.

https://doi.org/10.5194/acp-2019-879
Preprint. Discussion started: 12 November 2019
© Author(s) 2019. CC BY 4.0 License.

We developed the observation operators for OMPS SO_2 and NO_2, and the validations are shown in Fig. 1. The sensitivities of the cost function with respect to anthropogenic SO_2 and NO_x emissions from the adjoint model is consistent with the sensitivities calculated through the finite difference approach. Hence, Fig. 1 confirms the correctness of the new observation operators integrated into the GEOS-Chem adjoint model.

To optimize the emission inventories, $\boldsymbol{\sigma}$ is adjusted iteratively until the cost function is minimized. The minimization is conducted with the L-BFGS-B algorithm (Byrd et al., 1995), which utilizes the sensitivity of the cost function with respect to $\boldsymbol{\sigma}$ that is calculated by the GEOS-Chem adjoint model. The minimization process halts when the difference in the cost function between two consecutive iterations is less than 3%.

3.2 Experiment design

Several elements play a role in the inverse modeling of emissions, including data quality control, balancing the spatial distributions of observational frequencies for the same species, balancing the observation contributions from different species, and uncertainties in the NH_3 emission inventory (because NH_3 has impacts on SO_2 and NO_2 lifetimes). To investigate the impacts of these factors on the posterior emissions, we design a set of experiments as summarized in Table 1 and Table 2. All these experiments use OMPS SO_2 and NO_2 retrievals to optimize corresponding emissions over China in October 2013 at a horizontal resolution of 2°x2.5°. Although finer resolution options such as 0.5°x0.625° or 0.25°x0.3125° are available for China, the 2°x2.5° resolution is selected to save computational time; in Part II (Wang et al., 2019) of this study, we develop downscaling tools for regional air quality modeling.

3.2.1 Control experiments

The first control experiment is E-SO_2, in which only OMPS SO_2 tropospheric VCDs are used to constrain SO_2 emissions by removing the second additive term on the right side of Eq. (1). γ is just set to unity, as the issue of balancing the cost function contributions from SO_2 and NO_2 observations does not exist. If the OMPS SO_2 tropospheric VCD error is set to 0.2 DU (Yang et al., 2013) for every pixel, the SO_2 observational term in the cost function (first term on the right side of Eq. (1)) over the North China Plain is much larger than that over Southwestern China (Fig. 2b), which thus has the high potential to over-constrain the former and under-constrain the latter. The spatially unbalanced cost function is caused by cloud screening, as the number of observations over Southwestern China is much less than that over the North China Plain (Fig. 2a). To balance the cost function by accounting for this difference in the number of observation, SO_2 observation error is set to 0.2 DU multiplied by

https://doi.org/10.5194/acp-2019-879
Preprint. Discussion started: 12 November 2019
© Author(s) 2019. CC BY 4.0 License.
Atmospheric Chemistry and Physics
Discussions

the square root of the number of OMPS overpasses that have SO_2 observation in the 2°x2.5° GEOS-Chem grid cell.

In the E-NO_2 experiment, OMPS NO_2 tropospheric VCDs alone are used to constrain NO_x emissions by removing the first additive term on the right side of Eq. (1). Due to cloud screening, we have much more OMPS NO_2 observations over the North China Plain than over Southwestern China, which also could lead to a spatially unbalanced cost function if the OMPS NO_2 observation error is uniform. The OMPS NO_2 observation error is, however, assumed to be 0.011 DU (Yang et al., 2014) for every pixel in this study, regardless of location, because the NO_x emissions adjustments during the inverse modeling process are supposed to be mainly over the North China Plain where prior NO_x emissions are much larger than those over Southwestern China. In this study, we optimize emission scale factors rather than the emissions themselves, thus emissions are adjusted mainly at locations where prior emissions are large.

Both the SO_2 and NO_2 from OMPS are used simultaneously in E-joint for two reasons. Firstly, Qu et. al (2019b) showed that the change of SO_2 or NO_x emissions lead to the changes of O_3 and OH concentrations, hence the changes of SO_2 and NO_2 oxidations. Secondly, the computational time is reduced by ~50% in the joint assimilation as compared to separate assimilations when computational resource are restricted to running individual inversions sequentially (as opposed to in parallel), and energy usage is also saved; the latter require the realization of GEOS-chem adjoint twice, while only once is needed by the former.

In the E-joint experiment, observational terms for SO_2 and NO_2 in the cost function should be balanced through setting γ in Eq. (1). If they are not balanced, it is likely to under-constrain for one observational term. One approach is to set γ to be the ratio of number of NO_2 observations to the number of SO_2 observations. This approach is not feasible here as the SO_2 observational error in E-SO_2 is much larger than the NO_2 observational error in E-NO_2; not only does the number of observations play a role, but the observation error also has important impacts on balancing the cost function. If γ is simply set as unity, the NO_2 observational term in Eq. (1) is a factor of ~200 larger than the SO_2 observational term, which can lead to OMPS SO_2 in the E-joint experiment to be negligible. To balance the two terms, γ is set as 200 (ratio of observational term in E-NO_2 to that in E-SO_2) in E-joint.

3.2.2 Sensitivity experiments

https://doi.org/10.5194/acp-2019-879
Preprint. Discussion started: 12 November 2019
© Author(s) 2019. CC BY 4.0 License.

To investigate the impacts of data quality control and spatially balancing the cost function on optimizing SO_2 emissions only, we design two sensitivity experiments. The first is E-SO_2-noQC-noBL that is similar to E-SO_2 except that: (1) OMPS SO_2 retrievals in the 2°x2.5° grid cell where the prior GEOS-Chem simulation is less than 0.1 DU are also assimilated, i.e. without QC; (2) OMPS SO_2 observation error is set as 0.2 DU for every pixel, which means we do not spatially balance the cost function. The second sensitivity experiment is E-SO_2-noBL in which the cost function is not spatially balanced, and it uses the same setting as E-SO_2 except for assuming an observation error of 0.2 DU uniformly.

To evaluate the effect of γ (of 200) in E-joint, we further test γ values of 20, 50, 100, 300, 500, 1000, 1500, and 2000 in the joint inversions; hereafter these experiments are named E-joint-dγ. Through these sensitivity experiments, we study the proper γ range for jointly assimilating OMPS SO_2 and NO_2. In future studies that may be conducted to jointly assimilate OMPS SO_2 and NO_2 for other months to obtain a long-term optimized emission inventory, it is proposed to set proper γ values for each month based on the range with easy adjustment according to the numbers of OMPS SO_2 and NO_2 observations and their associated errors.

NH_3 emissions are not optimized in our inverse modeling and yet their uncertainty is up to 153% over China (Kurokawa et al., 2013). Thus, it is important to evaluate how this uncertainty may affect posterior SO_2 and NO_x emissions. Wang et al. (2013) emphasized the importance of controlling NH_3 to alleviate $PM_{2.5}$ pollution over China, however it could worsen acid rain (Liu et al., 2019). Changes of NH_3 emissions is expected to change ammonium and nitrate aerosol concentrations, or the aerosol surface area for heterogeneous N_2O_5 chemistry, hence affecting NO_2 concentrations or posterior NO_x emissions in the inverse modeling. The change of posterior NO_x emissions is expected to lead to the change of posterior SO_2 emissions in the joint inverse modeling. Thus, we shall investigate if NH_3 emissions are reduced to 50% and 20%, how the optimized SO_2 and NO_2 emission inventories would change. Correspondingly, all these experiments are summarized in Table 2. E-SO_2-0.5NH_3, E-NO_2-0.5NH_3, and E-joint-0.5NH_3-γ500 in Table 2 are similar to E-SO_2, E-NO_2, and E-joint-dγ (γ=500) in Table 1, respectively, but NH_3 emissions are set to 50% of the original values. Similarly, E-SO_2-0.2NH_3, E-NO_2-0.2NH_3, and E-joint-0.2NH_3- γ500 are the scenarios that NH_3 emissions are set to 20% of the original values.

3.3 Evaluation statistics

We use linear correlation coefficient (R), root mean square error (RMSE), mean bias (MB), normalized mean bias (NMB), normalized standard deviation (NSD), and normalized centered root mean square error (NCRMSE) as

https://doi.org/10.5194/acp-2019-879
Preprint. Discussion started: 12 November 2019
© Author(s) 2019. CC BY 4.0 License.

measures to evaluate GEOS-Chem SO_2 and NO_2 VCD simulations with satellite (OMPS and OMI) observations. NSD is the ratio of the standard deviation of the simulation to the standard deviation of the observation. NCRMSE is similar to RMSE, but the impact of bias is removed. This is shown in Eq. (2), where i is the i^{th} grid cell, N is the total number of grid cells, M_i and O_i are the i^{th} GEOS-Chem simulation and satellite observation, respectively, and $\bar{M}$ and $\bar{O}$ are averages of GEOS-Chem simulation and satellite observation, respectively. A composite summary of these statistics is provided by the Taylor diagram (Taylor, 2001) which is a quadrant which summarizes R (shown as cosine of polar angle), NSD (shown as radius from the quadrant center), and NCRMSE (shown as radius from expected, satellite observation, point, which is located at the point where R and NSD are unity).

$$\mathrm{NCRMSE} = \frac{\sqrt{\frac{1}{N}\sum_{i=1}^{N}[(M_i-\bar{M})-(O_i-\bar{O})]^2}}{\sqrt{\frac{1}{N}\sum_{i=1}^{N}(O_i-\bar{O})^2}} \qquad (2)$$

4. Results

4.1 Separate and joint assimilations of SO_2 and NO_2

4.1.1 Self-consistency check

The cost functions are reduced by 41.6%, 27.6%, and 28.6% for E-SO_2, E-NO_2, and E-joint, respectively, and the results are shown in Fig. 3. Noticeably, hot spots of SO_2 VCDs over the North China Plain and the Sichuan Basin are shown in the OMPS observations (Fig. 3a), prior (Fig. 3b), posterior E-SO_2 (Fig. 3c), and posterior E-joint (Fig. 3d) simulations, however the prior simulation has an NMB of 106.5% (Fig. 3i) when compared with OMPS. This large positive NMB decreases to 13.0% and 38.3% in the posterior E-SO_2 (Fig. 3j) and E-joint (Fig. 3k) simulations with an RMSE decreasing from 0.42 DU to 0.13 DU and 0.20 DU and R increasing from 0.62 to 0.72 and 0.64, respectively. Large NO_2 values are found over the North China Plain and Eastern China with large NO_x emissions from the transportation sector (Fig. 3e-h). Comparing with OMPS NO_2, GEOS-Chem results have an RMSE of 0.05 DU in the prior simulation (Fig. 3l) and reduce to 0.02 DU and 0.03 DU for E-NO_2 (Fig. 3m) and E-joint (Fig. 3n), with R increasing from 0.95 to 0.99 and 0.98, respectively. In general, the E-SO_2 and E-NO_2 posterior simulations show better results than E-joint, which may be affected by the value of γ, which we will discuss in Sect. 4.3.

4.1.2 Emissions

https://doi.org/10.5194/acp-2019-879
Preprint. Discussion started: 12 November 2019
© Author(s) 2019. CC BY 4.0 License.

The anthropogenic SO_2 and NO_x prior MIX emissions for October 2010 and posterior emissions from E-SO_2, E-NO_2, and E-joint for October 2013 are shown in Fig. 4. SO_2 and NO_x hot spots are found in the prior emissions over both the North China Plain and Eastern China, while large SO_2 emissions are also at Southwestern China. Anthropogenic SO_2 emissions over China are 1166 Gg S in prior MIX for October 2010 (Fig. 4a), dropping 418 Gg S (Fig. 4b) and 306 Gg S (Fig. 4c), or 35.8% and 26.2%, in E-SO_2 and E-joint for, respectively, for October 2013. Our finding of a large reduction of SO_2 emissions is in marked contrast with the 9% reduction from 2010 to 2013 analyzed in a bottom-up emission inventory from Zheng et al. (2018)'s research. The differences of reduction in percentage may imply overestimation of MIX SO_2 emissions for October 2010 or underestimation of this study for October. Posterior E-joint total anthropogenic SO_2 emissions are 112 Gg, or 15% larger than E-SO_2 over China (Fig. 4e), but the difference can be up to 100% in some model grid cells (Fig. 4f). Anthropogenic NO_x emissions over China are reduced by 5.8% and 6.5% , from 714 Gg N in prior MIX for October 2010 (Fig 4g) to 672 Gg N (Fig. 4h) in E-NO_2 and 667 Gg N (Fig. 4i) in E-joint for October 2013, although all other emissions inventories (Zheng et al., 2018; Miyazaki et al., 2017; Ding et al., 2017) reveal upward trends or no trends during the period. This sign difference may imply overestimation of MIX NO_x emissions for October 2010 or underestimation of this study for October. Although the relative difference between E-joint and E-NO_2 proved to be less than 2% in terms of total anthropogenic NO_x emissions over China (Fig. 4k), it is up to 40% for some model grid cells (Fig. 4 l).

4.1.3 Independent evaluation with OMI data

The optimized emission inventories are evaluated by comparing prior and posterior GEOS-Chem simulations of SO_2 and NO_2 with OMI VCDs as shown in Fig. 5. We only focus on regions covered by OMPS observations, although smaller changes of emissions exist in outskirt regions where OMPS observations are not used. High SO_2 levels are shown over the North China Plain and the Sichuan Basin in both the prior and posterior simulations while OMI only observes hot spots over the former region (Fig. 5a-d). When validating with OMI SO_2 VCDs, the NMB is ~300% in the prior simulation, and it reduces to ~100% in E-SO_2 and ~130% in E-joint (Fig. 5i). Not only is the NMB reduced, but the spatial distributions are also improved with the NCRMSE reducing from ~1.6 in the prior simulation to ~0.7 in E-SO_2 and ~0.8 in E-joint, which is much closer to ~0.6 when comparing OMPS observations with OMI observations (Fig. 5i). For NO_2, OMI observations and the prior and posterior simulations show large NO_2 concentrations over the North China Plain and Eastern China (Fig. 5e-h). The improvements for E-NO_2 and E-joint are reflected in terms of R when evaluating with OMI tropospheric VCDs, although the two experiments show larger negative NMB than the prior simulation (Fig. 5j).

https://doi.org/10.5194/acp-2019-879
Preprint. Discussion started: 12 November 2019
© Author(s) 2019. CC BY 4.0 License.

Although OMPS observations and GEOS-Chem simulations are compared with OMI observations as an evaluation of posterior emission inventories, it is not assumed that OMI provides the true status of SO_2 and NO_2 in the atmosphere. OMPS SO_2 average is ~0.14 DU, or ~95% larger than OMI SO_2, and the R of the two products is 0.81 (Fig. 6b). Thus, it is reasonable that posterior SO_2 is larger than OMI observations by ~100% in E-SO_2 and ~130% in E-joint. OMPS NO_2 is ~24% smaller than OMI (Fig. 6d), which explains why the posterior NO_2 simulations have larger negative NMB than the prior simulation when compared with the OMI observations. Our analysis also shows that the systematic difference among various satellite products for the same species (such as SO_2 or NO_2) can lead to biases in constraining emissions, but the posterior GEOS-Chem simulations still show in terms of the spatial distribution of SO_2 and NO_2.

4.2 The impacts of QC and spatial balance

The results of E-SO_2-noQC-noBL and E-SO_2-noBL are compared with E-SO_2 to show the impacts of QC and spatial balance. Both OMPS retrievals and the GEOS-Chem prior simulations show that SO_2 VCDs over Inner Mongolia and the Sichuan Basin (grid cells M and S, respectively in Fig. 7) are smaller than those over the North China Plain; this pattern reverses in the posterior E-SO_2-noQC-noBL simulation where SO_2 over the North China Plain becomes smaller than that over grid cells M and S. Grid cell M becomes more reasonable after conducting the data quality control by removing OMPS SO_2 in any grid cells where prior GEOS-Chem SO_2 VCDs are less than 0.1 DU (e.g., as in E-SO_2-noBL, as shown in Fig. 7d). QC helps to improve grid cell M, as the data removed are close to Inner Mongolia, and are generally less than 0.1 DU, which are comparable to the retrieval error. SO_2 over grid cell S from E-SO_2-noBL (Fig. 7d) is, however, still larger than that over the North China Plain, compared with the better spatial pattern from E-SO_2 (Fig. 3c). Thus, QC and spatial balancing of the cost function together improve the spatial pattern of the posterior GEOS-Chem SO_2 VCD simulation.

4.3 The impacts of γ on joint assimilations

In addition to setting γ as 200 in E-joint, we test the impacts of using various γ values on joint assimilation in E-joint-dγ for October 2013. All the SO_2 and NO_2 VCDs from prior and posterior E-joint and E-joint-dγ simulations are compared with OMPS counterparts (Fig. 8a-b). Regardless of the γ values used, all the posterior simulations of SO_2 show smaller NMB and NCRMSE than the prior simulation when validating against OMPS and OMI counterparts, but the extents vary. When γ is 20, 50, or 100, the SO_2 terms are obviously under-constrained, and GEOS-Chem SO_2 NCRMSE, evaluated with OMPS observations, changes from ~1.8 in the prior simulation to in the range of ~1.4 to ~1.7 in the posterior E-joint-dγ simulations, which are much larger than ~0.7 in E-SO_2 (Fig. 8a). Similarly, when γ is no larger than 100, the bias of GEOS-Chem SO_2, validated with OMPS observations, only reduces from ~100% to ~75%, compared to ~25% in E-SO_2 (Fig. 8a), and the posterior SO_2 emissions are in the range of 1055 Gg S to 1143 Gg S, which are much larger than 748 Gg S from E-SO_2 (Table 3). When γ is in the range of 200 to 2000, the SO_2 simulation results and emissions from joint assimilations are more similar to that from E-SO_2 than that with γ no larger than 100 (Fig. 8a and Table 3). Similar to SO_2, the NO_2 GEOS-Chem simulations in the sensitivity experiments improve in terms of R and NCRMSE in all joint assimilation tests, but the significance of γ is less than that for SO_2. NO_2 NCRMSE is ~0.4 in the prior simulation when evaluating with OMPS counterparts, compared to the range of ~0.2 to ~0.25 in E-joint, E-joint-dγ and E-NO_2 (Fig. 8b). The posterior NO_x emissions are in the range of 662 Gg N to 682 Gg N, compared with 672 Gg N in E-NO_2 (Table 3).

The impacts of γ are also reflected when evaluating SO_2 and NO_2 simulations with OMI retrievals (Fig. 8c-d). Small γ values of 20, 50, and 100 lead to a much larger bias and NCRMES for SO_2 from E-joint-dγ than that from E-SO_2. For NO_2, these small γ values make results from E-joint-dγ very similar to that from E-NO_2.

Considering all of the above analyses, the results with γ in the range of 200 to 2000 are deemed acceptable. The E-joint-dγ (200≤ γ ≤2000) emissions are within -3% to 15% of E-SO_2 for SO_2 and ±2% of E-NO_2 for NO_x in terms of total anthropogenic SO_2 and NO_x emissions over China. When evaluating with OMPS observations, the NCRMSE of using the posterior emissions from the separate and joint (200≤ γ ≤2000) inversions are ~60% and ~45%-60% smaller than that of using the prior emissions for SO_2, respectively, and ~50% and ~38%-50% smaller than that of using the prior emissions for NO_2, respectively.

4.4 The impacts of NH_3 emission

In the single-species inversions, NH_3 emission uncertainty has weaker impacts on posterior SO_2 emissions than NO_x emissions. Posterior SO_2 emissions over China are 748 Gg S in the 100% NH_3 emission scenario (E-SO_2), and they only slightly reduce to 747 Gg S and 745 Gg S when NH_3 emissions are 50% (E-SO_2-0.5NH_3) and 20% (E-SO_2-0.2NH_3) of the original values, respectively (Table 4). The largest relative changes at model-grid-cell scale are only -2.5% (Fig. 9a) for E-SO_2-0.5NH_3 for and -4.7% (Fig. 9b) for E-SO_2-0.2NH_3. All these results can be explained by considering how changes of NH_3 can potentially impact the lifetimes of SO_2 and NO_2 and hence affect SO_2 and NO_2 VCD simulations. When the NH_3 emissions decrease to 50%, and 20% SO_2 VCDs only increase up to 3.8% and 6.1%, respectively, in some grid cells over the Sichuan Basin in the prior simulations, and these changes are even much smaller over the North China Plain (Fig. 10a-b), as NH_3 has no direct effect on the life cycle of SO_2. This is understandable because in GEOS-Chem, once SO_2 is oxidized to H_2SO_4, SO_4^{2-} remains as particulate sulfate regardless it is neutralized by NH_3 or not (Wang et al., 2008). Hence, the reductions of NH_3 to 50% and 20% overall has minimal (negligible) impact on SO_2 amount in the prior simulation, hence on the posterior separate SO_2 emission inversion.

Although the posterior NO_x emissions in the scenarios of 50% (E-NO_2-0.5NH_3) and 20% (E-NO_2-0.2NH_3) NH_3 emission experiments of the original values are 5 Gg N (0.7%) and 19 Gg N (2.8%), respectively, which are smaller than those when using the original (E-NO_2) NH_3 emissions over China (Table 4), the reduction is up to -4.0% (Fig. 9e) for E-NO_2-0.5NH_3 and -9.1% (Fig. 9f) for E-NO_2-0.2NH_3 in individual grid cells. These decreases are understood by simultaneous reduction of nitrate by 59.5% (Fig. 12h vs. 12g) and 80.5% (Fig 12i vs. 12g) and ammonium by 39.6% (Fig. 12n vs. 12m) and 67.5% (Fig. 12o vs. 12m), which leads to large reduction of the hydrated aerosol surface area for heterogeneous N_2O_5 chemistry at night, hence overall NO_2 lifetime (Fig. 10c-d). N_2O_5 normally forms at night by reaction between NO_2 and NO_3, and thermally decomposes back to NO_2 and NO_3 (Seinfeld and Pandis, 2016), and hence the amount of N_2O_5, NO_2, and NO_3 are in equilibrium through the reversible reaction. Since the hydrolysis of N_2O_5 to form HNO_3 mainly occurs on hydrated aerosol particles (Seinfeld and Pandis, 2016), the decrease of hydrated aerosol surface area (due to reduction of NH_3 emission) leads to less hydrolysis of N_2O_5 (an important sink for atmospheric NOx) and subsequently more NO_2 to be in the equilibrium with N_2O_5 at night. As a result, the reduction of NH_3 emissions further increases the positive bias in the prior NO_2 simulations when comparing with OMPS observations, and to compensate such large positive bias, non-negligible decreases in the posterior NO_x emissions are required (Fig. 9 e and f). The reduction of nitrate and ammonium aerosols can also increase sunlight reaching troposphere, hence photolysis O_3 and NO_2. Figure S1 separates the impacts of increase of photolysis O_3 and NO_2 and decrease heterogeneous N_2O_5 chemistry on NO_2 lifetime and shows that the former is negligible compared the latter.

The decreases of posterior SO_2 and NO_x emissions in the joint inversions caused by the reduction of NH_3 emissions are stronger than that in the separate inversions (Table 4 and Fig. 9). Although the changes of NH_3 emissions only have slight impacts on the SO_2 separate inversions (E-SO_2, E-SO_2-0.5NH_3, and E-SO_2-0.2NH_3), the posterior SO_2 emission is 802 Gg S in E-joint-dγ (γ=500), down to 783 Gg S (decreasing by 2.4%) and 746 Gg S (decreasing by 7.0%) in E-joint-0.5NH_3- γ500 and E-joint-0.2NH_3- γ500, respectively (Table 4); in some grid cells, the relative reductions are up to -9.0% (Fig. 9c) for E-joint-0.5NH_3- γ500 and -27.7% (Fig. 9d) for E-

https://doi.org/10.5194/acp-2019-879
Preprint. Discussion started: 12 November 2019
© Author(s) 2019. CC BY 4.0 License.

joint-0.2NH_3- γ500. For posterior NO_x emissions at the grid cells, the relative changes are up -15.2% (Fig. 9g) for E-joint-0.5NH_3- γ500 and -29.4% (Fig. 9h) for E-joint-0.2NH_3- γ500 with respect to E-joint-dγ (γ=500).

4.5 Aerosol responses to emission changes

Although SO_2 emissions over the North China Plain (E-joint-dγ (γ=500)) have decreased by more than 50%, and NO_x emissions have also been reduced, reductions of Sulfate-Nitrate-Ammonium (SNA) Aerosol Optical Depth (AOD) over the same region are only up to 10% (Fig. 11). This is because the North China Plain is mainly polluted by nitrate rather than sulfate (Fig. 12a-l), and the reduction of SO_2 emissions will increase nitrate loadings in the atmosphere (Fig. 12g-l), which is also consistent with Kharol et al. (2013)'s research that shows nitrate concentrations decrease as SO_2 emissions increase; the reduction of SO_2 emissions lead to less H_2SO_4 to react with NH_3, which further favor the reaction of HNO_3 and NH_3 to form nitrate. As NH_3 emissions change reduce by 50% and 80% ammonium column loadings decrease by ~40% and ~70% (Fig. 12g-l), respectively, and nitrate column loadings decrease even by ~70% and ~90%, respectively (Fig. 12m-r).

5. Discussion and conclusions

We develop 4D-var observation operators for assimilating OMPS SO_2 and NO_2 VCDs to constrain SO_2 and NO_x emissions through GEOS-Chem adjoint model. The approach is applied for case study in China for October 2013 at 2°x2.5° resolution and the MIX 2010 is used as the prior emission inventory. Several experiments of assimilating OMPS SO_2 and NO_2 separately and jointly are conducted, and SO_2 and NO_2 VCDs from the GEOS-Chem prior and posterior simulations are compared with counterparts from OMPS and OMI.

OMPS SO_2 and NO_2 retrievals are separately and jointly used to constrain their corresponding emissions. In the single-species inversions, posterior anthropogenic SO_2 and NO_x emissions are 748 Gg S and 672 Gg N for October 2013, down from 1166 Gg S and 714 Gg N in the prior MIX for October 2010, respectively. In the joint inversions of assimilating OMPS SO_2 and NO_2 simultaneously, the cost function is balanced according to the values of observational terms rather than the number of observations. When the cost function is well balanced (γ in the range of 200 to 2000), the results of the joint inversions are within -3% to 15% of the single-species inversion for total anthropogenic SO_2 emissions and ±2% for total anthropogenic NO_x emissions. However, the differences between the separate and joint inversions are up to 100% and 40% in some model grid cells for anthropogenic SO_2 and NO_x emissions, respectively. In comparison to OMPS observations, NCRMSE from joint inversions (γ

https://doi.org/10.5194/acp-2019-879
Preprint. Discussion started: 12 November 2019
© Author(s) 2019. CC BY 4.0 License.

in the range of 200 to 2000) is reduced by ~45%-~60% for SO_2 and ~38%-~50% for NO_2, respectively, which is close to the ~60% reduction from the SO_2 inversion and the ~50% reduction from the separate NO_2 inversion. To obtain posterior emissions for both SO_2 and NO_x, the computational time for the joint inversion is only about ~50% of the single-species inversions, when the latter are computed sequentially. Moreover, posterior GEOS-Chem SO_2 and NO_2 show improvements in terms of R when comparing against OMI observations, and the increase of posterior GEOS-Chem NO_2 negative NMB is ascribed to that the average of OMPS NO_2 over China is smaller than the OMI counterpart. Above all, the posterior emission increases the GEOS-Chem simulated spatial distributions of SO_2 and NO_2.

Both data quality control and spatially balancing the cost function play an important role for constraining SO_2 emissions. OMPS SO_2 retrievals over the regions where emissions are small are removed as VCDs are comparable to retrieval errors. A sensitivity study shows that if these data are included, it will lead to artifacts in the posterior SO_2 emission spatial distribution. Due to cloud screening, the number of OMPS SO_2 retrievals over the Sichuan Basin is much less than that over the North China Plain, which will lead to under-constraining over Sichuan Basin, if the observation error is assumed spatially constant. When the observation error is set based on the number of observations, the artifacts are avoided.

To investigate the impacts of the uncertainty of NH_3 emissions on posterior SO_2 and NO_x emissions, several inverse modeling experiments are conducted by setting prior NH_3 emissions to as 50% and 20% of their original values. The reduction of NH_3 emissions can lead to a larger decrease of posterior NO_x emissions and a smaller decrease of SO_2 emissions in separate assimilations, which ascribes to the NO_2 lifetime is more than the SO_2 affected by the change of NH_3 emissions. The impacts of NH_3 emissions uncertainty on both posterior SO_2 and NO_x emissions in joint assimilations are stronger than separate assimilations.

Large SO_2 emissions are mainly produced over the Sichuan basin and the North China Plain, while AOD responses to the changes of SO_2 emissions are quite different over the two regions. The reduction in SO_2 emissions can effectively decrease AOD over the Sichuan Basin, while AOD declines only slightly over the North China Plain, which can be ascribed to (1) nitrate rather than sulfate is dominant over the North China Plain and (2) the reduction of SO_2 emissions facilitate the formation of additional nitrate. AOD over the North China Plain is mainly determined by NO_x and NH_3 emissions rather than SO_2 emissions.

https://doi.org/10.5194/acp-2019-879
Preprint. Discussion started: 12 November 2019
© Author(s) 2019. CC BY 4.0 License.
Atmospheric Chemistry and Physics Discussions

All emissions are constrained on the monthly scale and at the coarse spatial resolution of 2°x2.5° in this study, as OMPS observations are provided once per day and the 4D-Var data assimilation at finer spatial resolution (on the order of 0.1 degree) would be computationally prohibitive. The approach, however, has the potential for optimizing emissions at the daily resolution from higher temporal resolution observations, such as those from future geostationary satellites. In particular, TEMPO (monitoring North America), GEMS (monitoring East Asia), and Sentinel-4 (monitoring Europe) are to be launched in the next several years, and all of these satellites will provide hourly SO_2 and NO_2 observations during the daytime. Furthermore, in Part II of this work, we develop various downscale methods to apply these coarser-resolution top-down estimates of emissions for air quality forecasts and evaluate the forecasts with surface measurements, both at the finer spatial scale (Wang et al., 2019).

Author contributions. All authors designed the research; YW conducted the research; YW and JW wrote the paper; XX, DKH and ZQ contributed to writing.

Competing interests. The authors declare that they have no conflict of interest.

Acknowledgements. This research is supported by the National Aeronautics and Space Administration (NASA) through ACMAP program (grant numbers: NNX17AF77G and 80NSSC19K0950) managed by Richard Eckman, and through TEMPO project as part of NASA's Earth Venture program (grant number SV7-87011 subcontracted from Harvard Smithsonian Observatory to the University of Iowa). We acknowledge the computational support from the High-Performance Computing group at The University of Iowa and Prof. Charles O. Stanier from The University of Iowa for insightful comments on the analysis of SO_2 and NO_2 lifetimes.

References

Bucsela, E. J., Celarier, E. A., Gleason, J. L., Krotkov, N. A., Lamsal, L. N., Marchenko, S. V., and Swartz, W. H.: OMNO2 README Document Data Product Version 3.0, 2016.

Byrd, R., Lu, P., Nocedal, J., and Zhu, C.: A Limited Memory Algorithm for Bound Constrained Optimization, SIAM J. Sci. Comput., 16, 1190-1208, doi:10.1137/0916069, 1995.

Calkins, C., Ge, C., Wang, J., Anderson, M., and Yang, K.: Effects of meteorological conditions on sulfur dioxide air pollution in the North China plain during winters of 2006–2015, Atmos. Environ., 147, 296-309, https://doi.org/10.1016/j.atmosenv.2016.10.005, 2016.

Cooper, M., Martin, R. V., Padmanabhan, A., and Henze, D. K.: Comparing mass balance and adjoint methods for inverse modeling of nitrogen dioxide columns for global nitrogen oxide emissions, J. Geophys. Res., 122, 4718-4734, 10.1002/2016JD025985, 2017.

Ding, J., Miyazaki, K., van der A, R. J., Mijling, B., Kurokawa, J. I., Cho, S., Janssens-Maenhout, G., Zhang, Q., Liu, F., and Levelt, P. F.: Intercomparison of NOx emission inventories over East Asia, Atmos. Chem. Phys., 17, 10125-10141, 10.5194/acp-17-10125-2017, 2017.

Ding, J., van der A, R. J., Mijling, B., Levelt, P. F., and Hao, N.: NO_x emission estimates during the 2014 Youth Olympic Games in Nanjing, Atmos. Chem. Phys., 15, 9399-9412, 10.5194/acp-15-9399-2015, 2015.

Fioletov, V. E., McLinden, C. A., Krotkov, N., Yang, K., Loyola, D. G., Valks, P., Theys, N., Van Roozendael, M., Nowlan, C. R., Chance, K., Liu, X., Lee, C., and Martin, R. V.: Application of OMI, SCIAMACHY, and GOME-2 satellite SO_2 retrievals for detection of large emission sources, J. Geophys. Res., 118, 2013JD019967, 10.1002/jgrd.50826, 2013.

Fioletov, V. E., McLinden, C. A., Krotkov, N., Li, C., Joiner, J., Theys, N., Carn, S., and Moran, M. D.: A global catalogue of large SO_2 sources and emissions derived from the Ozone Monitoring Instrument, Atmos. Chem. Phys., 16, 11497-11519, 10.5194/acp-16-11497-2016, 2016.

Flynn, L., Long, C., Wu, X., Evans, R., Beck, C. T., Petropavlovskikh, I., McConville, G., Yu, W., Zhang, Z., Niu, J., Beach, E., Hao, Y., Pan, C., Sen, B., Novicki, M., Zhou, S., and Seftor, C.: Performance of the Ozone Mapping and Profiler Suite (OMPS) products, J. Geophys. Res., 119, 6181-6195, 10.1002/2013JD020467, 2014.

Henze, D. K., Hakami, A., and Seinfeld, J. H.: Development of the adjoint of GEOS-Chem, Atmos. Chem. Phys., 7, 2413-2433, 10.5194/acp-7-2413-2007, 2007.

Janssens-Maenhout, G., Crippa, M., Guizzardi, D., Dentener, F., Muntean, M., Pouliot, G., Keating, T., Zhang, Q., Kurokawa, J., Wankmüller, R., Denier van der Gon, H., Kuenen, J. J. P., Klimont, Z., Frost, G., Darras, S., Koffi, B., and Li, M.: HTAP_v2.2: a mosaic of regional and global emission grid maps for 2008 and 2010 to study hemispheric transport of air pollution, Atmos. Chem. Phys., 15, 11411-11432, 10.5194/acp-15-11411-2015, 2015.

Kharol, S. K., Martin, R. V., Philip, S., Vogel, S., Henze, D. K., Chen, D., Wang, Y., Zhang, Q., and Heald, C. L.: Persistent sensitivity of Asian aerosol to emissions of nitrogen oxides, Geophys. Res. Lett., 40, 1021-1026, 10.1002/grl.50234, 2013.

Kong, H., Lin, J., Zhang, R., Liu, M., Weng, H., Ni, R., Chen, L., Wang, J., and Zhang, Q.: High-resolution (0.05°×0.05°) NOx emissions in the Yangtze River Delta inferred from OMI, Atmos. Chem. Phys. Discuss., 2019, 1-39, 10.5194/acp-2018-1275, 2019.

Koukouli, M. E., Theys, N., Ding, J., Zyrichidou, I., Mijling, B., Balis, D., and van der A, R. J.: Updated SO_2 emission estimates over China using OMI/Aura observations, Atmos. Meas. Tech., 11, 1817-1832, 10.5194/amt-11-1817-2018, 2018.

Krotkov, N. A., Lamsal, L. N., Celarier, E. A., Swartz, W. H., Marchenko, S. V., Bucsela, E. J., Chan, K. L., Wenig, M., and Zara, M.: The version 3 OMI NO2 standard product, Atmos. Meas. Tech., 10, 3133-3149, 10.5194/amt-10-3133-2017, 2017.

Kurokawa, J., Ohara, T., Morikawa, T., Hanayama, S., Janssens-Maenhout, G., Fukui, T., Kawashima, K., and Akimoto, H.: Emissions of air pollutants and greenhouse gases over Asian regions during 2000–2008: Regional Emission inventory in ASia (REAS) version 2, Atmos. Chem. Phys., 13, 11019-11058, 10.5194/acp-13-11019-2013, 2013.

Kurokawa, J.-i., Yumimoto, K., Uno, I., and Ohara, T.: Adjoint inverse modeling of NO_x emissions over eastern China using satellite observations of NO_2 vertical column densities, Atmos. Environ., 43, 1878-1887, http://dx.doi.org/10.1016/j.atmosenv.2008.12.030, 2009.

Lamsal, L. N., Martin, R. V., van Donkelaar, A., Celarier, E. A., Bucsela, E. J., Boersma, K. F., Dirksen, R., Luo, C., and Wang, Y.: Indirect validation of tropospheric nitrogen dioxide retrieved from the OMI satellite instrument: Insight into the seasonal variation of nitrogen oxides at northern midlatitudes, J. Geophys. Res., 115, 10.1029/2009JD013351, 2010.

Lamsal, L. N., Martin, R. V., Padmanabhan, A., van Donkelaar, A., Zhang, Q., Sioris, C. E., Chance, K., Kurosu, T. P., and Newchurch, M. J.: Application of satellite observations for timely updates to global anthropogenic NOx emission inventories, Geophys. Res. Lett., 38, L05810, 10.1029/2010GL046476, 2011.

Lee, C., Martin, R. V., van Donkelaar, A., Lee, H., Dickerson, R. R., Hains, J. C., Krotkov, N., Richter, A., Vinnikov, K., and Schwab, J. J.: SO_2 emissions and lifetimes: Estimates from inverse modeling using in situ and global, space-based (SCIAMACHY and OMI) observations, J. Geophys. Res., 116, D06304, 10.1029/2010JD014758, 2011.

Lelieveld, J., Evans, J. S., Fnais, M., Giannadaki, D., and Pozzer, A.: The contribution of outdoor air pollution sources to premature mortality on a global scale, Nature, 525, 367-371, 10.1038/nature15371, 2015.

© Author(s) 2019. CC BY 4.0 License.

Leonard, J. T.: README for OMSO2e (OMI Daily L3e for OMSO2) Version 1.1.7, https://acdisc.gesdisc.eosdis.nasa.gov/data/Aura_OMI_Level3/OMSO2e.003/doc/README.OMSO2e.pdf, 2017.

Li, C., Joiner, J., Krotkov, N. A., and Bhartia, P. K.: A fast and sensitive new satellite SO_2 retrieval algorithm based on principal component analysis: Application to the ozone monitoring instrument, Geophys. Res. Lett., 40, 6314-6318, 10.1002/2013GL058134, 2013.

Li, C., Krotkov, N. A., Carn, S., Zhang, Y., Spurr, R. J. D., and Joiner, J.: New-generation NASA Aura Ozone Monitoring Instrument (OMI) volcanic SO_2 dataset: algorithm description, initial results, and continuation with the Suomi-NPP Ozone Mapping and Profiler Suite (OMPS), Atmos. Meas. Tech., 10, 445-458, 10.5194/amt-10-445-2017, 2017a.

Li, M., Zhang, Q., Kurokawa, J. I., Woo, J. H., He, K., Lu, Z., Ohara, T., Song, Y., Streets, D. G., Carmichael, G. R., Cheng, Y., Hong, C., Huo, H., Jiang, X., Kang, S., Liu, F., Su, H., and Zheng, B.: MIX: a mosaic Asian anthropogenic emission inventory under the international collaboration framework of the MICS-Asia and HTAP, Atmos. Chem. Phys., 17, 935-963, 10.5194/acp-17-935-2017, 2017b.

Lim, S. S., Vos, T., Flaxman, A. D., Danaei, G., Shibuya, K., Adair-Rohani, H., AlMazroa, M. A., Amann, M., Anderson, H. R., Andrews, K. G., Aryee, M., Atkinson, C., Bacchus, L. J., Bahalim, A. N., Balakrishnan, K., Balmes, J., Barker-Collo, S., Baxter, A., Bell, M. L., Blore, J. D., Blyth, F., Bonner, C., Borges, G., Bourne, R., Boussinesq, M., Brauer, M., Brooks, P., Bruce, N. G., Brunekreef, B., Bryan-Hancock, C., Bucello, C., Buchbinder, R., Bull, F., Burnett, R. T., Byers, T. E., Calabria, B., Carapetis, J., Carnahan, E., Chafe, Z., Charlson, F., Chen, H., Chen, J. S., Cheng, A. T.-A., Child, J. C., Cohen, A., Colson, K. E., Cowie, B. C., Darby, S., Darling, S., Davis, A., Degenhardt, L., Dentener, F., Des Jarlais, D. C., Devries, K., Dherani, M., Ding, E. L., Dorsey, E. R., Driscoll, T., Edmond, K., Ali, S. E., Engell, R. E., Erwin, P. J., Fahimi, S., Falder, G., Farzadfar, F., Ferrari, A., Finucane, M. M., Flaxman, S., Fowkes, F. G. R., Freedman, G., Freeman, M. K., Gakidou, E., Ghosh, S., Giovannucci, E., Gmel, G., Graham, K., Grainger, R., Grant, B., Gunnell, D., Gutierrez, H. R., Hall, W., Hoek, H. W., Hogan, A., Hosgood Iii, H. D., Hoy, D., Hu, H., Hubbell, B. J., Hutchings, S. J., Ibeanusi, S. E., Jacklyn, G. L., Jasrasaria, R., Jonas, J. B., Kan, H., Kanis, J. A., Kassebaum, N., Kawakami, N., Khang, Y.-H., Khatibzadeh, S., Khoo, J.-P., Kok, C., Laden, F., Lalloo, R., Lan, Q., Lathlean, T., Leasher, J. L., Leigh, J., Li, Y., Lin, J. K., Lipshultz, S. E., London, S., Lozano, R., Lu, Y., Mak, J., Malekzadeh, R., Mallinger, L., Marcenes, W., March, L., Marks, R., Martin, R., McGale, P., McGrath, J., Mehta, S., Memish, Z. A., Mensah, G. A., Merriman, T. R., Micha, R., Michaud, C., Mishra, V., Hanafiah, K. M., Mokdad, A. A., Morawska, L., Mozaffarian, D., Murphy, T., Naghavi, M., Neal, B., Nelson, P. K., Nolla, J. M., Norman, R., Olives, C., Omer, S. B., Orchard, J., Osborne, R., Ostro, B., Page, A., Pandey, K. D., Parry, C. D. H., Passmore, E., Patra, J., Pearce, N., Pelizzari, P. M., Petzold, M., Phillips, M. R., Pope, D., Pope Iii, C. A., Powles, J., Rao, M., Razavi, H., Rehfuess, E. A., Rehm, J. T., Ritz, B., Rivara, F. P., Roberts, T., Robinson, C., Rodriguez-Portales, J. A., Romieu, I., Room, R., Rosenfeld, L. C., Roy, A., Rushton, L., Salomon, J. A., Sampson, U., Sanchez-Riera, L., Sanman, E., Sapkota, A., Seedat, S., Shi, P., Shield, K., Shivakoti, R., Singh, G. M., Sleet, D. A., Smith, E., Smith, K. R., Stapelberg, N. J. C., Steenland, K., Stöckl, H., Stovner, L. J., Straif, K., Straney, L., Thurston, G. D., Tran, J. H., Van Dingenen, R., van Donkelaar, A., Veerman, J. L., Vijayakumar, L., Weintraub, R., Weissman, M. M., White, R. A., Whiteford, H., Wiersma, S. T., Wilkinson, J. D., Williams, H. C., Williams, W., Wilson, N., Woolf, A. D., Yip, P., Zielinski, J. M., Lopez, A. D., Murray, C. J. L., and Ezzati, M.: A comparative risk assessment of burden of disease and injury attributable to 67 risk factors and risk factor clusters in 21 regions, 1990–2010: a systematic analysis for the Global Burden of Disease Study 2010, The Lancet, 380, 2224-2260, http://dx.doi.org/10.1016/S0140-6736(12)61766-8, 2012.

Liu, F., Zhang, Q., van der A., R., J., Zheng, B., Tong, D., Yan, L., Zheng, Y., and He, K.: Recent reduction in NO_x emissions over China: synthesis of satellite observations and emission inventories, Environ. Res. Lett., 11, 114002, 2016.

Liu, F., Choi, S., Li, C., Fioletov, V. E., McLinden, C. A., Joiner, J., Krotkov, N. A., Bian, H., Janssens-Maenhout, G., Darmenov, A. S., and da Silva, A. M.: A new global anthropogenic SO_2 emission inventory for the last decade: a mosaic of satellite-derived and bottom-up emissions, Atmos. Chem. Phys., 18, 16571-16586, 10.5194/acp-18-16571-2018, 2018.

Liu, H., Jacob, D. J., Bey, I., and Yantosca, R. M.: Constraints from 210Pb and 7Be on wet deposition and transport in a global three-dimensional chemical tracer model driven by assimilated meteorological fields, J. Geophys. Res., 106, 12109-12128, 10.1029/2000JD900839, 2001.

Liu, M., Huang, X., Song, Y., Tang, J., Cao, J., Zhang, X., Zhang, Q., Wang, S., Xu, T., Kang, L., Cai, X., Zhang, H., Yang, F., Wang, H., Yu, J. Z., Lau, A. K. H., He, L., Huang, X., Duan, L., Ding, A., Xue, L., Gao, J., Liu, B., and Zhu, T.: Ammonia emission control in China would mitigate haze pollution and nitrogen deposition, but worsen acid rain, Proceedings of the National Academy of Sciences, 201814880, 10.1073/pnas.1814880116, 2019.

© Author(s) 2019. CC BY 4.0 License.

Marchenko, S., Krotkov, N. A., Lamsal, L. N., Celarier, E. A., Swartz, W. H., and Bucsela, E. J.: Revising the slant column density retrieval of nitrogen dioxide observed by the Ozone Monitoring Instrument, J. Geophys. Res., 120, 5670-5692, 10.1002/2014JD022913, 2015.

Martin, R. V., Jacob, D. J., Chance, K., Kurosu, T. P., Palmer, P. I., and Evans, M. J.: Global inventory of nitrogen oxide emissions constrained by space-based observations of NO_2 columns, J. Geophys. Res., 108, 4537, 10.1029/2003JD003453, 2003.

Mijling, B., and van der A, R. J.: Using daily satellite observations to estimate emissions of short-lived air pollutants on a mesoscopic scale, J. Geophys. Res., 117, 10.1029/2012JD017817, 2012.

Miyazaki, K., Eskes, H. J., and Sudo, K.: Global NOx emission estimates derived from an assimilation of OMI tropospheric NO_2 columns, Atmos. Chem. Phys., 12, 2263-2288, 10.5194/acp-12-2263-2012, 2012.

Miyazaki, K., Eskes, H., Sudo, K., Boersma, K. F., Bowman, K., and Kanaya, Y.: Decadal changes in global surface NOx emissions from multi-constituent satellite data assimilation, Atmos. Chem. Phys., 17, 807-837, 10.5194/acp-17-807-2017, 2017.

Miyazaki, K., Eskes, H., Sudo, K., Boersma, K. F., Bowman, K., and Kanaya, Y.: Decadal changes in global surface NO_x emissions from multi-constituent satellite data assimilation, Atmos. Chem. Phys., 17, 807-837, 10.5194/acp-17-807-2017, 2017.

Myhre, G., Shindell, D., Bréon, F.-M., Collins, W., Fuglestvedt, J., Huang, J., Koch, D., Lamarque, J.-F., Lee, D., Mendoza, B., Nakajima, T., Robock, A., Stephens, G., Takemura, T., and Zhang, H.: Anthropogenic and Natural Radiative Forcing, in: Climate Change 2013: The Physical Science Basis. Contribution of Working Group I to the Fifth Assessment Report of the Intergovernmental Panel on Climate Change, edited by: Stocker, T. F., Qin, D., Plattner, G.-K., Tignor, M., Allen, S. K., Boschung, J., Nauels, A., Xia, Y., Bex, V., and Midgley, P. M., Cambridge University Press, Cambridge, United Kingdom and New York, NY, USA, 659–740, 2013.

Park, R. J., Jacob, D. J., Field, B. D., Yantosca, R. M., and Chin, M.: Natural and transboundary pollution influences on sulfate-nitrate-ammonium aerosols in the United States: Implications for policy, J. Geophys. Res., 109, D15204, 10.1029/2003JD004473, 2004.

Qu, Z., Henze, D. K., Capps, S. L., Wang, Y., Xu, X., Wang, J., and Keller, M.: Monthly top-down NO_x emissions for China (2005–2012): A hybrid inversion method and trend analysis, J. Geophys. Res., 122, 4600-4625, 10.1002/2016JD025852, 2017.

https://doi.org/10.5194/acp-2019-879
Preprint. Discussion started: 12 November 2019
© Author(s) 2019. CC BY 4.0 License.

Qu, Z., Henze, D. K., Li, C., Theys, N., Wang, Y., Wang, J., Wang, W., Han, J., Shim, C., Dickerson, R. R., and Ren, X.: SO_2 emission estimates using OMI SO_2 retrievals for 2005-2017, J. Geophys. Res., 0, 10.1029/2019JD030243, 2019a.

Qu, Z., Henze, D. K., Theys, N., Wang, J., and Wang, W.: Hybrid mass balance/4D-Var joint inversion of NO_x and SO_2 emissions in East Asia, J. Geophys. Res., 0, 10.1029/2018JD030240, 2019b.

Schenkeveld, V. M. E., Jaross, G., Marchenko, S., Haffner, D., Kleipool, Q. L., Rozemeijer, N. C., Veefkind, J. P., and Levelt, P. F.: In-flight performance of the Ozone Monitoring Instrument, Atmos. Meas. Tech., 10, 1957-1986, 10.5194/amt-10-1957-2017, 2017.

Seinfeld, J. H., and Pandis, S. N.: Atmospheric Chemistry and Physics: From Air Pollution to Climate Change, 3rd ed., Wiley, 2016.

Taylor, K. E.: Summarizing multiple aspects of model performance in a single diagram, J. Geophys. Res., 106, 7183-7192, 10.1029/2000JD900719, 2001.

Turner, A. J., Henze, D. K., Martin, R. V., and Hakami, A.: The spatial extent of source influences on modeled column concentrations of short-lived species, Geophys. Res. Lett., 39, n/a-n/a, 10.1029/2012GL051832, 2012.

Wang, Y., Jacob, D. J., and Logan, J. A.: Global simulation of tropospheric O_3-NO_x-hydrocarbon chemistry: 1. Model formulation, J. Geophys. Res., 103, 10713-10725, 10.1029/98JD00158, 1998.

Wang, Y., Zhang, Q. Q., He, K., Zhang, Q., and Chai, L.: Sulfate-nitrate-ammonium aerosols over China: response to 2000–2015 emission changes of sulfur dioxide, nitrogen oxides, and ammonia, Atmos. Chem. Phys., 13, 2635-2652, 10.5194/acp-13-2635-2013, 2013.

Wang, Y., Wang, J., Xu, X., Henze, D. K., Wang, Y., and Qu, Z.: A new approach for monthly updates of anthropogenic sulfur dioxide emissions from space: Application to China and implications for air quality forecasts, Geophys. Res. Lett., 43, 9931-9938, 10.1002/2016GL070204, 2016.

Wang, Y., Wang, J., Henze, D. K., Zhou, M., Ge, C., and Wang, W.: Inverse modeling of SO_2 and NO_x emissions over China from multi-sensor satellite data: 2. Downscaling for air quality forecasts Atmos. Chem. Phys., 2019.(submitted)

Wesely, M. L.: Parameterization of surface resistances to gaseous dry deposition in regional-scale numerical models, Atmospheric Environment (1967), 23, 1293-1304, http://dx.doi.org/10.1016/0004-6981(89)90153-4, 1989.

https://doi.org/10.5194/acp-2019-879
Preprint. Discussion started: 12 November 2019
© Author(s) 2019. CC BY 4.0 License.
Atmospheric Chemistry and Physics Discussions

Xu, X., Wang, J., Henze, D. K., Qu, W., and Kopacz, M.: Constraints on aerosol sources using GEOS-Chem adjoint and MODIS radiances, and evaluation with multisensor (OMI, MISR) data, J. Geophys. Res., 118, 6396-6413, 10.1002/jgrd.50515, 2013.

Yang, K., Dickerson, R. R., Carn, S. A., Ge, C., and Wang, J.: First observations of SO_2 from the satellite Suomi NPP OMPS: Widespread air pollution events over China, Geophys. Res. Lett., 40, 4957-4962, 10.1002/grl.50952, 2013.

Yang, K., Carn, S. A., Ge, C., Wang, J., and Dickerson, R. R.: Advancing measurements of tropospheric NO_2 from space: New algorithm and first global results from OMPS, Geophys. Res. Lett., 41, 4777-4786, 10.1002/2014GL060136, 2014.

Zhang, Y., Li, C., Krotkov, N. A., Joiner, J., Fioletov, V., and McLinden, C.: Continuation of long-term global SO2 pollution monitoring from OMI to OMPS, Atmos. Meas. Tech., 10, 1495-1509, 10.5194/amt-10-1495-2017, 2017.

Zheng, B., Tong, D., Li, M., Liu, F., Hong, C., Geng, G., Li, H., Li, X., Peng, L., Qi, J., Yan, L., Zhang, Y., Zhao, H., Zheng, Y., He, K., and Zhang, Q.: Trends in China's anthropogenic emissions since 2010 as the consequence of clean air actions, Atmos. Chem. Phys., 18, 14095-14111, 10.5194/acp-18-14095-2018, 2018.

https://doi.org/10.5194/acp-2019-879
Preprint. Discussion started: 12 November 2019
© Author(s) 2019. CC BY 4.0 License.
Atmospheric Chemistry and Physics Discussions
Open Access
EGU

Table 1. Different experimental design for using OMPS SO_2 and NO_2 to constrain corresponding emissions over China for October 2013.

Name	Data	SO_2 error[b]	NO_2 error	γ[c]	QC for SO_2[d]
E-SO_2	SO_2	0.2 DU x $\sqrt{N}$	NA	1	Yes
E-NO_2	NO_2	NA	0.011 DU	NA	NA
E-joint	SO_2 and NO_2	0.2 DU x $\sqrt{N}$	0.011 DU	200	Yes
E-SO_2-noQC-noBL	SO_2	0.2 DU	NA	1	No
E-SO_2-noBL	SO_2	0.2 DU	NA	1	Yes
E-joint-dγ	SO_2 and NO_2	0.2 DU x $\sqrt{N}$	0.011 DU	20 to 2000[e]	Yes

[a]See description of these names in detail in Set. 3.2.

[b]N in this column is number of OMPS overpass that have SO_2 observation in the 2x2.5 GEOS-Chem grid cell.

[c]γ is a parameter used to balance SO_2 and NO_2 observation terms in the cost function.

[d]OMPS SO_2 retrievals in the 2x2.5 grid cell where the prior GEOS-Chem simulation is less than 0.1 DU are removed.

[e]All these γ values (20, 50, 100, 300, 500, 1000, 1500, and 2000) are used.

https://doi.org/10.5194/acp-2019-879
Preprint. Discussion started: 12 November 2019
© Author(s) 2019. CC BY 4.0 License.

Table 2. Different experimental design for assessing the impacts of NH_3 emission inventories on using OMPS SO_2 and NO_2 to constrain corresponding emissions over China for October 2013[a].

Name[b]	Data	γ[c]	NH_3 emissions
E-SO_2-0.5NH_3	SO_2	NA	50%
E-NO_2-0.5NH_3	NO_2	NA	50%
E-joint-0.5NH_3- γ500	SO_2 and NO_2	500	50%
E-SO_2-0.2NH_3	SO_2	NA	20%
E-NO_2-0.2NH_3	NO_2	NA	20%
E-joint-0.2NH_3- γ500	SO_2 and NO_2	500	20%

[a]Data quality control and observation errors are same as E-joint in Table 1.

[b]See description of these names in detail in Set. 3.2.

[c]γ is a parameter used to balance SO_2 and NO_2 observation terms in the cost function.

https://doi.org/10.5194/acp-2019-879
Preprint. Discussion started: 12 November 2019
© Author(s) 2019. CC BY 4.0 License.
Atmospheric Chemistry and Physics
Discussions

Table 3. Posterior anthropogenic emissions for October 2013 from E-joint, E-joint-dγ, E-SO_2 and E-NO_2.

Experiment name or γ	20	50	100	200	300	500	1000	1500	2000	E-SO_2 or E-NO_2
SO_2 [Gg S]	1143	1110	1055	860	795	802	733	730	728	748
NO_x [Gg N]	681	682	682	667	662	664	668	666	674	672

https://doi.org/10.5194/acp-2019-879
Preprint. Discussion started: 12 November 2019
© Author(s) 2019. CC BY 4.0 License.
Atmospheric Chemistry and Physics Discussions
Open Access
EGU

Table 4. Posterior anthropogenic emissions for October 2013 under different NH_3 emission scenarios

Name	SO_2 emissions [Gg S]	NO_x emission [Gg N]
E-SO_2	748	NA
E-SO_2-0.5NH_3	747	NA
E-SO_2-0.2NH_3	745	NA
E-NO_2	NA	672
E-NO_2-0.5NH_3	NA	667
E-NO_2-0.2NH_3	NA	653
E-joint-dγ (γ=500)	802	664
E-joint-0.5NH_3- γ500	783	646
E-joint-0.2NH_3- γ500	746	629

© Author(s) 2019. CC BY 4.0 License.

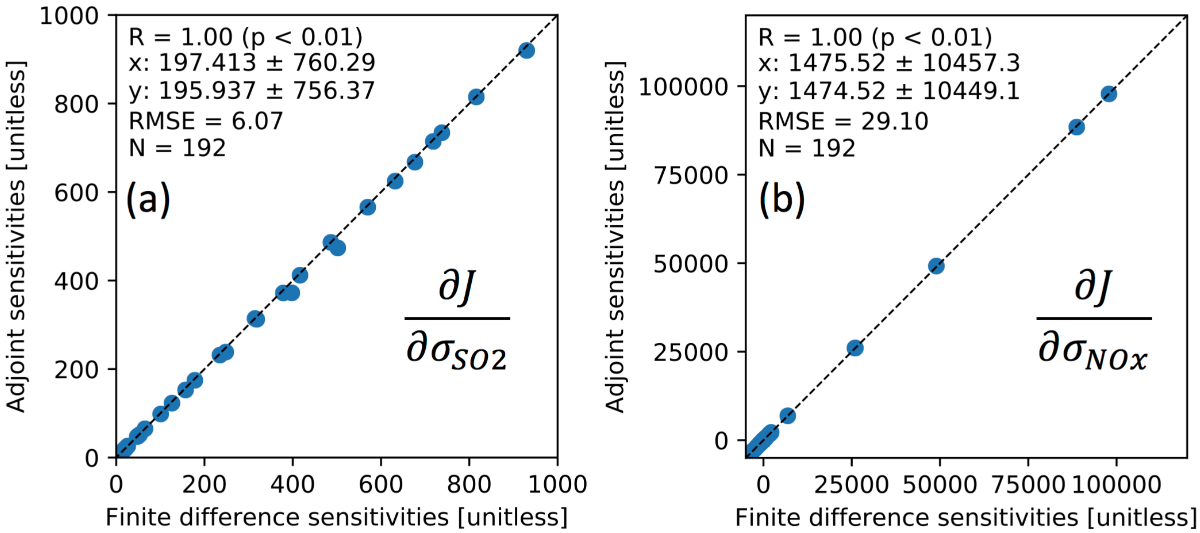

Figure 1. Validation of adjoint model sensitivity through comparison to centered finite difference results for a 3-day simulation. Shown here are the sensitivity of column cost function (penalty term is not included, and horizontal transport is turned off) with respect to logarithm of anthropogenic SO_2 (a) and NO_x (b) emission scale factors: the 1:1 line (dotted), the number of grid columns (N), Root Mean Squared Error (RMSE), and correlation coefficient (R), and Means and standard deviations of finite difference sensitivity and adjoint sensitivity (x and y).

© Author(s) 2019. CC BY 4.0 License.

Atmospheric Chemistry and Physics
Discussions

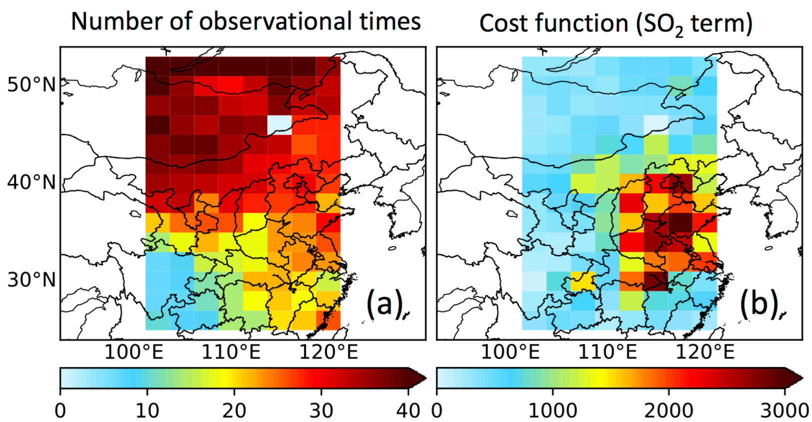

755 **Figure 2. (a) and (b) are the numbers of the OMPS overpass time that provides SO_2 VCD retrievals and SO_2 term in cost function at first iteration, respectively, in October 2013**

https://doi.org/10.5194/acp-2019-879
Preprint. Discussion started: 12 November 2019
© Author(s) 2019. CC BY 4.0 License.

Atmospheric Chemistry and Physics
Discussions

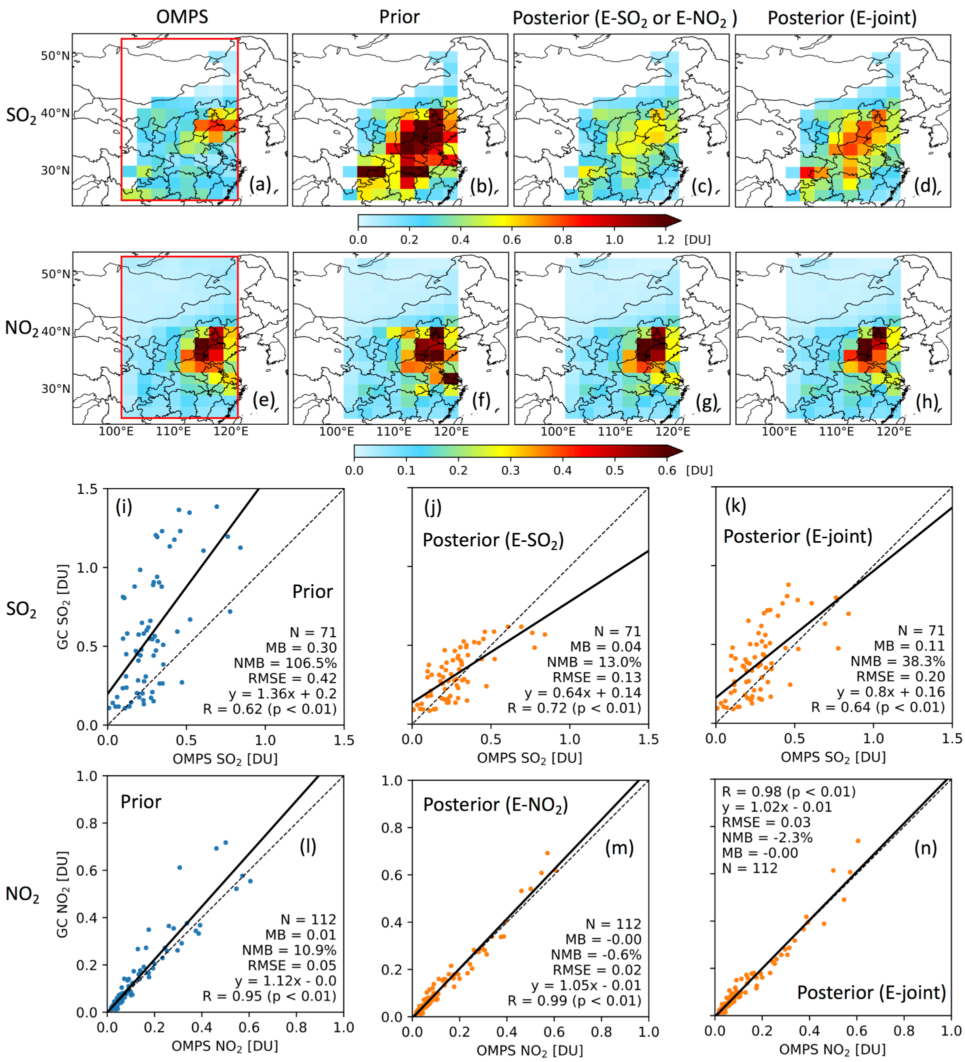

Figure 3. Comparisons of VCDs of SO_2 and NO_2 from the OMPS and the GEOS-Chem prior and posterior simulations in October 2013 over China. The first row is SO_2 VCDs from the OMPS (a), the prior simulation (b), the E-SO_2 posterior simulation (c), and the E-joint posterior simulation (d). The second row is NO_2 tropospheric VCDs from the OMPS (e), the prior simulation (f), the E-NO_2 posterior simulation (g), and the E-joint posterior simulation (h). The third row is the SO_2 VCD scatter plots of the GEOS-Chem prior (i), the E-SO_2 posterior (j), and the E-joint posterior (k) versus the OMPS, respectively. The last row is the NO_2 tropospheric VCD scatter plots of the GEOS-Chem prior (l), the E-NO_2 posterior (m), and the E-joint posterior (n) versus the OMPS, respectively. Linear correlation coefficient (R), linear regression equation, root mean squared error (RMSE), normalized mean bias (NMB), mean bias (MB), and number of observations (N) are shown over scatter plots.

https://doi.org/10.5194/acp-2019-879
Preprint. Discussion started: 12 November 2019
© Author(s) 2019. CC BY 4.0 License.

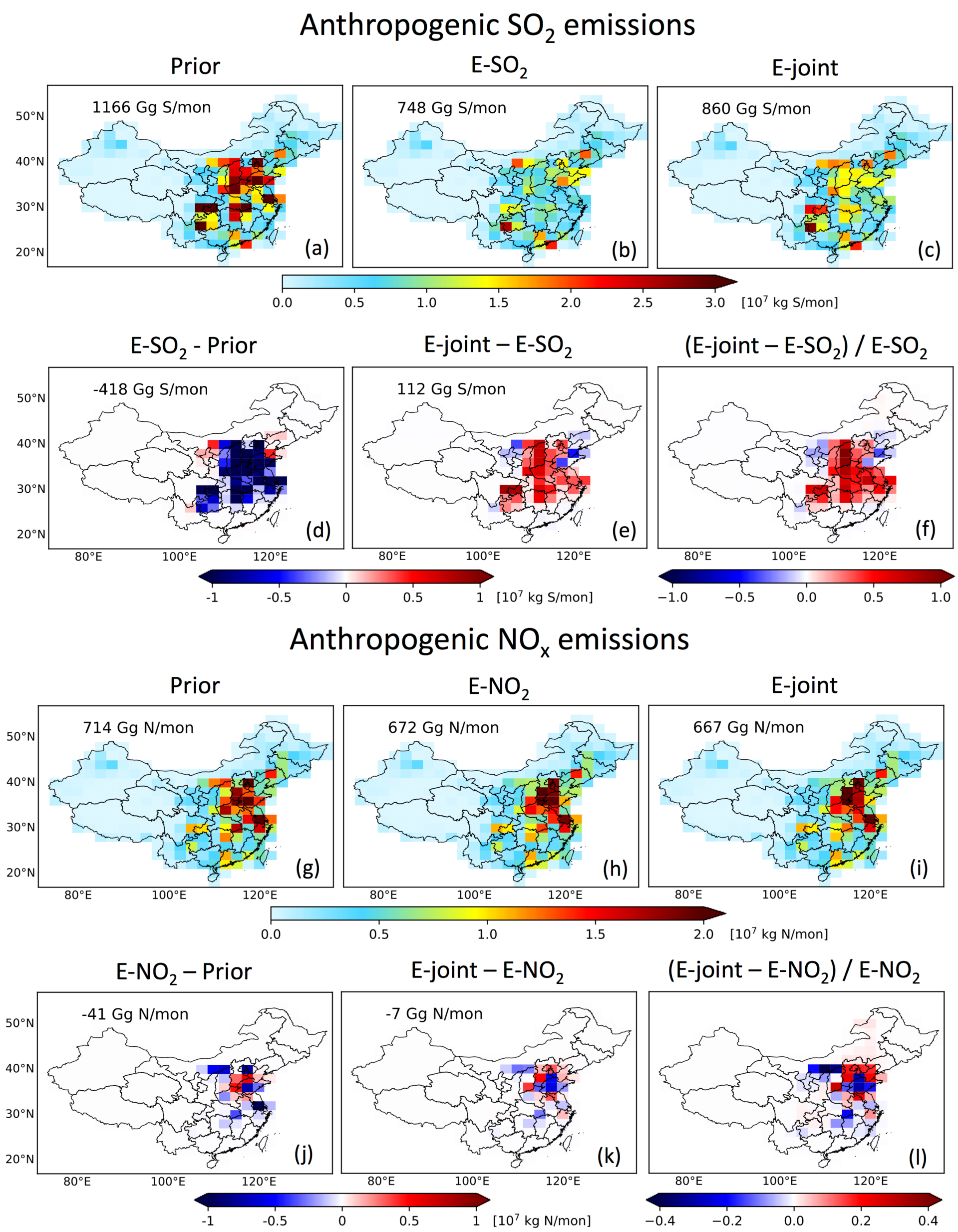

Figure 4. The top is anthropogenic SO_2 emissions from prior MIX 2010 (a), posterior E-SO_2 (b), posterior E-joint (c), the difference between posterior E-SO_2 and prior MIX 2010 (d), the difference between posterior E-joint and posterior E-SO_2 (e), and the relative difference between posterior E-joint and posterior E-SO_2 (f) for October 2013. The bottom is similar to the top except that (1) it is for NO_x and (2) E-SO_2 is replaced by E-NO_2.

https://doi.org/10.5194/acp-2019-879
Preprint. Discussion started: 12 November 2019
© Author(s) 2019. CC BY 4.0 License.
Atmospheric Chemistry and Physics
Discussions

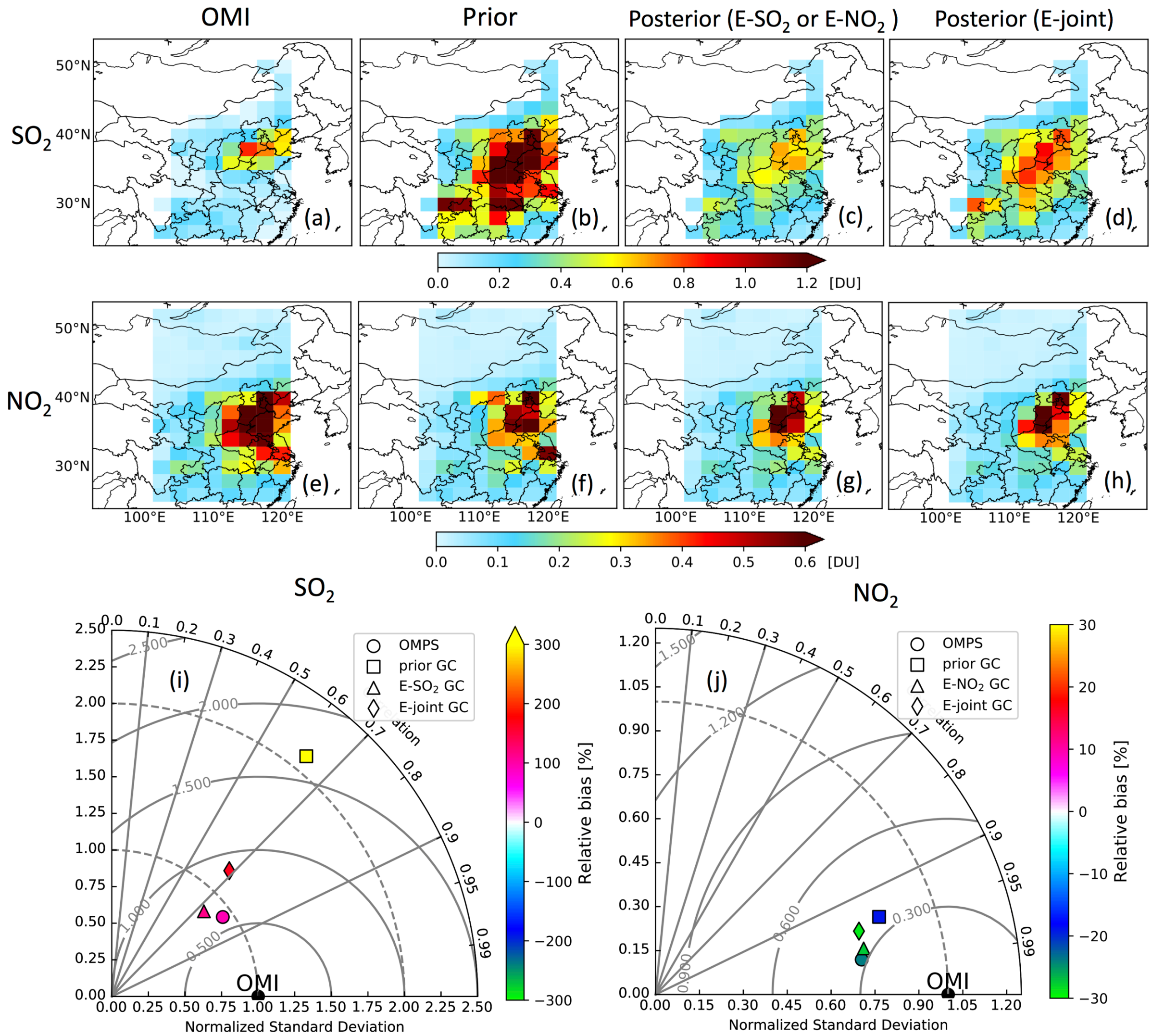

Figure 5. Comparisons of VCDs of SO_2 and NO_2 from the OMPS and the GEOS-Chem prior and posterior simulations with that from the OMI in October 2013 over China. The first row is SO_2 VCDs from the OMI (a), the prior simulation (b), the E-SO_2 posterior simulation (c), and the E-joint posterior simulation (d). The second row is NO_2 tropospheric VCDs from the OMI (e), the prior simulation (f), the E-NO_2 posterior simulation (g), and the E-joint posterior simulation (h). The third row is Taylor diagrams for comparing GEOS-Chem simulations (squares for prior, triangles for posterior E-SO2 or E-NO2, and diamonds for E-joint) and OMPS observations (circles) with OMI SO_2 (i) and NO_2 (j).

https://doi.org/10.5194/acp-2019-879
Preprint. Discussion started: 12 November 2019
© Author(s) 2019. CC BY 4.0 License.

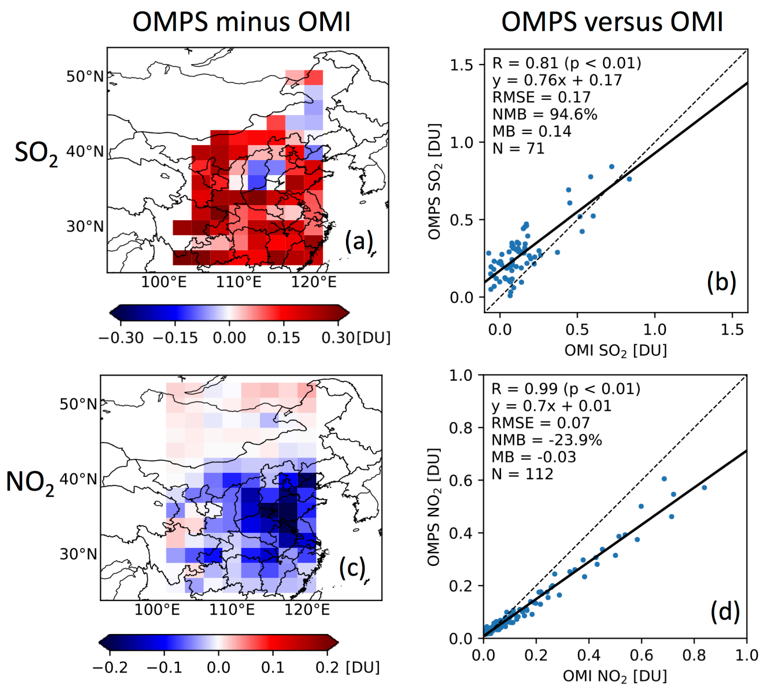

Figure 6. (a) and (b) are the difference between OMPS and OMI SO_2 and scatter plot of OMPS versus OMI SO_2. (c) and (d) are similar (a) and (b), but for NO_2. Linear correlation coefficient (R), linear regression equation, root mean squared error (RMSE), normalized mean bias (NMB), mean bias (MB), and number of observations (N) are shown over scatter plots.

https://doi.org/10.5194/acp-2019-879
Preprint. Discussion started: 12 November 2019
© Author(s) 2019. CC BY 4.0 License.
Atmospheric Chemistry and Physics Discussions

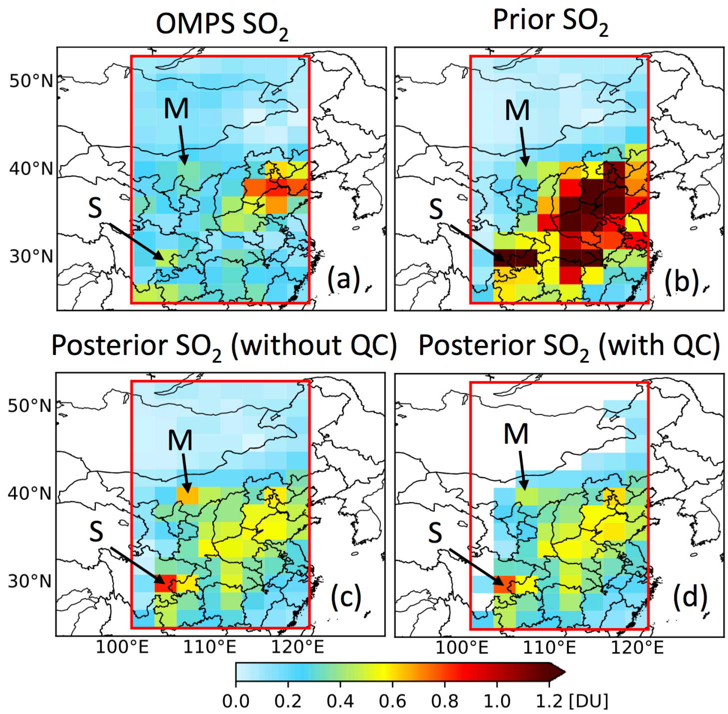

Figure 7. SO_2 VCD in October 2013 from OMPS (a), prior GEOS-Chem simulation (b), posterior GEOS-chem simulation through using all OMPS data in the red box (c), and posterior GEOS-chem simulation through using only OMPS data that are in the grid cell where GEOS-Chem prior simulation of VCD is larger than 0.1 DU. For posterior simulation, we only plot SO_2 VCD over grid cells where OMPS data are used to constrain emissions. M and S point to a grid cell in Inner Mongolia and Sichuan basin, respectively.

https://doi.org/10.5194/acp-2019-879
Preprint. Discussion started: 12 November 2019
© Author(s) 2019. CC BY 4.0 License.
Atmospheric Chemistry and Physics
Discussions

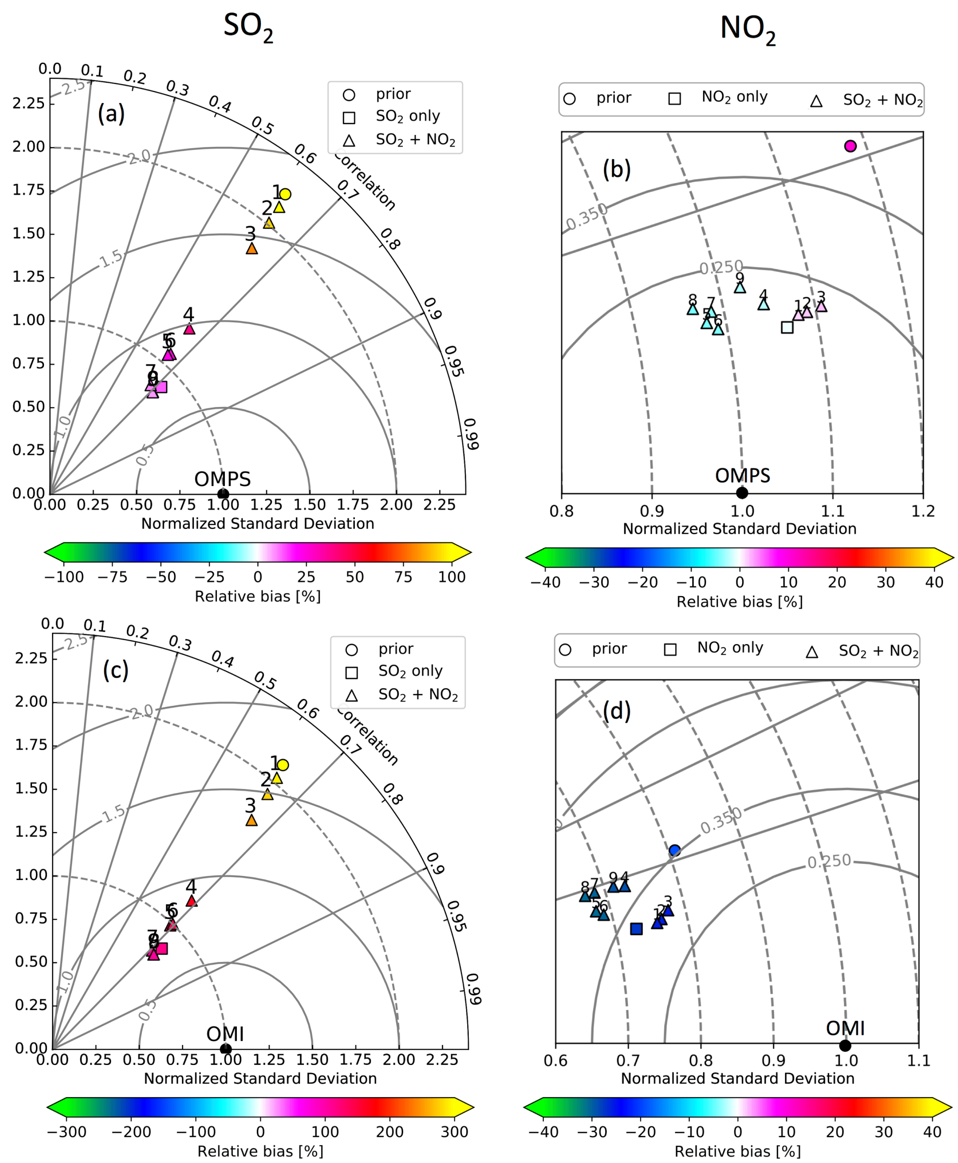

810 **Figure 8. Taylor diagram of comparing GEOS-Chem simulation with OMPS (a for SO_2 and b for NO_2) or OMI (c for SO_2 and d for NO_2) in October 2013. Circles, squares, and triangles represent GEOS-Chem simulations using prior MIX 2010 emissions, posterior emissions constrained by single species (E_SO2 for a and c, E_NO2 for b and d), and posterior emissions constrained through joint inversion (E_joint), respectively. Different triangles labeled by numbers represent different γ values in Eq. (1), and 1 through 9 correspond to 20, 50, 100, 200, 300, 500, 1000, 1500, and 2000, respectively.**

https://doi.org/10.5194/acp-2019-879
Preprint. Discussion started: 12 November 2019
© Author(s) 2019. CC BY 4.0 License.
Atmospheric Chemistry and Physics
Open Access
Discussions

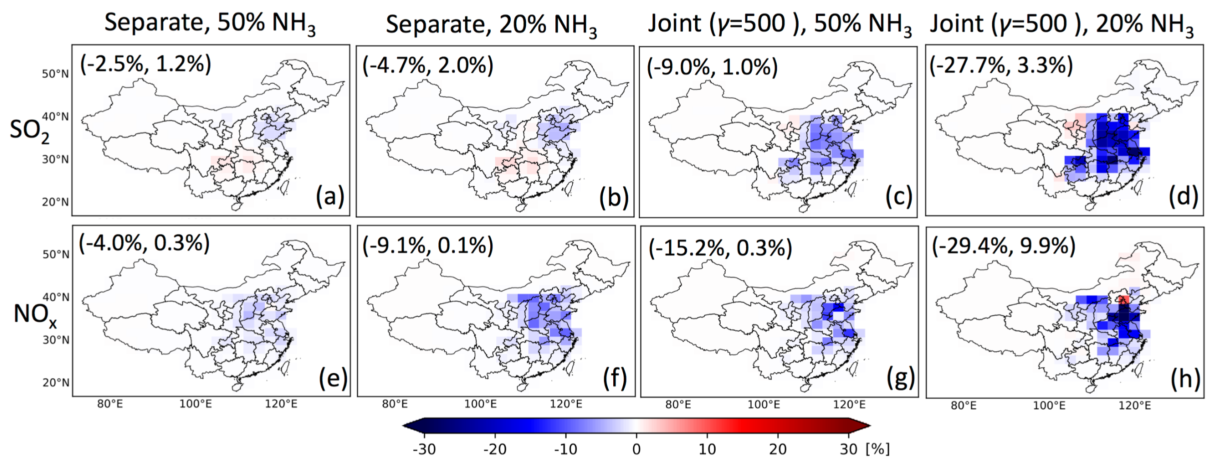

Figure 9. Relative changes of posterior SO_2 (top row) and NO_x (bottom row) emissions from the scenarios of perturbing NH_3 emissions with respect to that using original NH_3 emission inventory. (a) and (b) are relative changes of posterior SO_2 emissions from E-SO_2-0.5NH_3 and E-SO_2-0.2NH_3 with respect to that from E-SO_2, respectively. (c) and (d) are relative changes of posterior SO_2 emissions from E-joint-0.5NH_3-γ500 and E-joint-0.2NH_3-γ500 with respect to that from E-joint-dγ (γ=500), respectively. (e) and (f) are relative changes of posterior NO_x emissions from E-NO_2-0.5NH_3 and E-NO_2-0.2NH_3 with respect to that from E-NO_2, respectively. (g) and (h) are similar to (c) and (d), respectively, but for posterior NO_x emissions. Minimum and maximum are shown in brackets.

https://doi.org/10.5194/acp-2019-879
Preprint. Discussion started: 12 November 2019
© Author(s) 2019. CC BY 4.0 License.

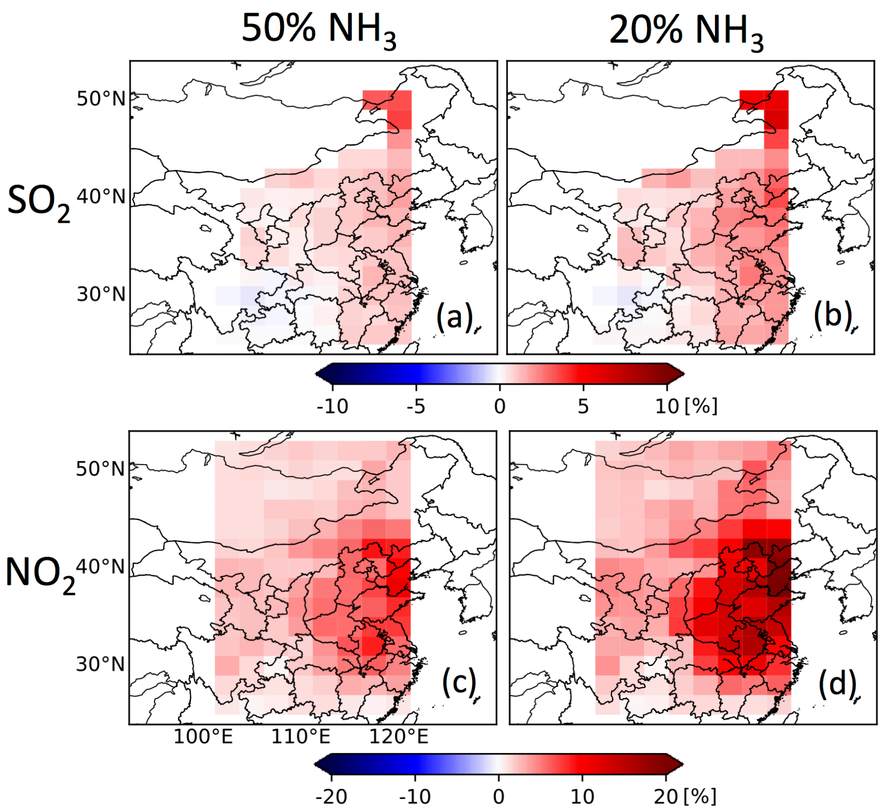

830 **Figure 10. Relative change of GEOS-Chem SO_2 VCDs when NH_3 emissions reduce to 50% (a) and 20% (b), respectively at OMPS overpassing time. (c) and (d) are similar to (a) and (b), respectively, but for NO_2.**

https://doi.org/10.5194/acp-2019-879
Preprint. Discussion started: 12 November 2019
© Author(s) 2019. CC BY 4.0 License.
Atmospheric Chemistry and Physics Discussions

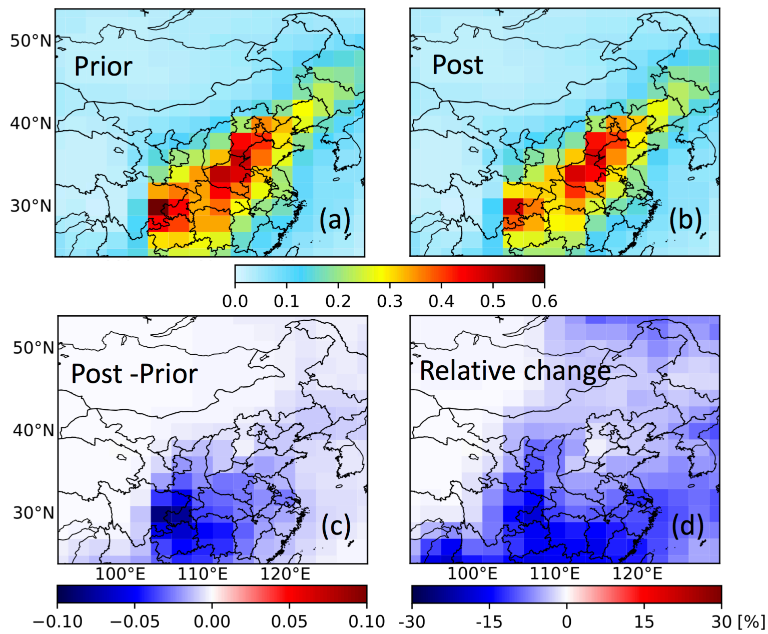

835 **Figure 11. Sulfate-nitrate-ammonium aerosol optical depth in prior (a) and posterior joint inversion (γ=500) (b). (c) is the difference between (b) and (a), and (d) is relative change in percentage.**

https://doi.org/10.5194/acp-2019-879
Preprint. Discussion started: 12 November 2019
© Author(s) 2019. CC BY 4.0 License.

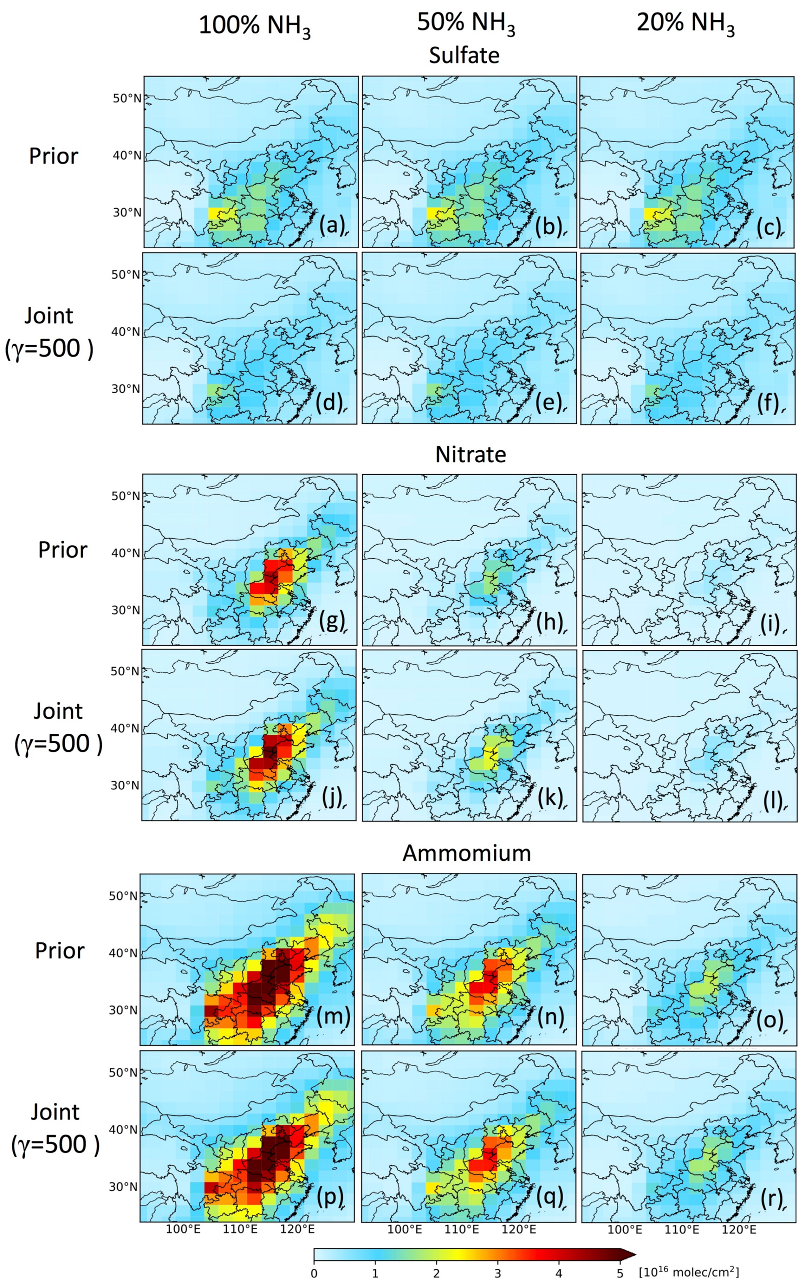

840 **Figure 12. Sulfate, nitrate, and ammonium column loadings in different scenarios. (a), (b), and (c) are prior sulfate at 100%, 50%, and 20% NH_3 emissions, respectively. (d), (e), and (f) are posterior sulfate from joint inversions (γ=500) at 100%, 50%, and 20% NH_3 emissions, respectively. (g)-(i) and (m)-(r) are similar to (a)-(f), but for nitrate and ammonium, respectively.**